Three-Dimensional Electrical Conductivity and Induced Polarization Tomography of a Rock Glacier

P. Duvillard, A. Revil, Y. Qi, A Soueid Ahmed, A. Coperey, Ludovic Ravanel, A. Soueid Ahmed

▶ **To cite this version:**

P. Duvillard, A. Revil, Y. Qi, A Soueid Ahmed, A. Coperey, et al.. Three-Dimensional Electrical Conductivity and Induced Polarization Tomography of a Rock Glacier. Journal of Geophysical Research : Solid Earth, 2018, 123 (11), pp.9528-9554. 10.1029/2018JB015965 . hal-02324265

HAL Id: hal-02324265
https://hal.science/hal-02324265

Submitted on 23 Nov 2020

HAL is a multi-disciplinary open access archive for the deposit and dissemination of scientific research documents, whether they are published or not. The documents may come from teaching and research institutions in France or abroad, or from public or private research centers.

L'archive ouverte pluridisciplinaire **HAL**, est destinée au dépôt et à la diffusion de documents scientifiques de niveau recherche, publiés ou non, émanant des établissements d'enseignement et de recherche français ou étrangers, des laboratoires publics ou privés.

Journal of Geophysical Research: Solid Earth

RESEARCH ARTICLE
10.1029/2018JB015965

Three-Dimensional Electrical Conductivity and Induced Polarization Tomography of a Rock Glacier

P. A. Duvillard[1,2], A. Revil[3], Y. Qi[3], A. Soueid Ahmed[3], A. Coperey[3], and L. Ravanel[1]

[1]Université Grenoble Alpes Université Savoie Mont-Blanc, CNRS, UMR CNRS 5204, EDYTEM, Le Bourget du Lac, France, [2]IMSRN, Montbonnot-Saint-Martin, France, [3]Université Grenoble Alpes, Université Savoie Mont Blanc, CNRS, IRD, IFSTTAR, ISTerre, Grenoble, France

Key Points:
- Induced polarization of rock glacier is investigated. During freeze and thaw, rocks show two polarization effects
- Surface conductivity controls the rock electrical conductivity of rocks during freeze and thaw
- An experiment and a field study on an Alpine rock glacier are performed to investigate the electrical conduction in freezing conditions

Correspondence to:
A. Revil,
andre.revil@univ-smb.fr

Citation:
Duvillard, P. A., Revil, A., Qi, Y., Soueid Ahmed, A., Coperey, A., & Ravanel, L. (2018). Three-dimensional electrical conductivity and induced polarization tomography of a rock glacier. *Journal of Geophysical Research: Solid Earth*, *123*. https://doi.org/10.1029/2018JB015965

Received 15 APR 2018
Accepted 23 OCT 2018
Accepted article online 29 OCT 2018

Abstract Three-dimensional electrical resistivity and induced polarization data were collected on an unstable Alpine rock glacier in Val Thorens (Vanoise massif, France). In addition to these field data, we also performed induced polarization measurements during freeze and thaw using a soil sample and the poorly mineralized water, both from this site. In the tomograms, the electrical conductivity and the normalized chargeability show very distinctly the presence of the rock ice mixture. The chargeability itself is however quite constant over the entire investigated area with the exception of a small area associated with the presence of carboniferous rocks rich in graphite. The background chargeability is close to the dimensionless number $R = 8 \times 10^{-2}$, which is consistent with the prediction of the dynamic Stern layer model for the polarization of porous media. The theory implies that this dimensionless number R is independent on saturation and temperature in agreement with field observations. A main implication of this observation is that the classical Archie's law cannot be applied to describe the electrical conductivity in this type of environments with poorly mineralized pore water. Surface conductivity dominates the measured conductivity of the materials implying in turn that the electrical conductivity is related to both the water content and cation exchange capacity of the material. We propose new equations for both the electric conductivity and the normalized chargeability in this type of environments.

Plain Language Summary Induced polarization is a geophysical method looking at imaging the 3D distribution of properties related to the ability of rocks to store reversibly electrical charges under the application of a primary electrical field. This method has never been applied to rock glaciers. A field application and a laboratory experiment demonstrate the usefulness of this method to characterize Alpine rock glaciers and point up some shortcomings in the interpretation of electrical conductivity tomography done by previous authors in this type of environments.

1. Introduction

Climate change is currently causing substantial changes in the cryosphere, for instance leading to critical morphological responses of glaciers and rock glaciers in high mountain areas like in the Alps (Beniston et al., 2018; Scherrer et al., 2016). The term *rock glacier* indicates rock debris located in the permafrost area where the interstitial spaces of the subsurface are mainly filled with ice or even supersaturated with ice. The creep of this mixture of debris and ice along the slope gives to the rock glaciers their typical morphology, generally characterized by a tongue-shaped appearance and transverse or longitudinal ridges and furrows related to the compression or extension of the material (Haeberli et al., 2006). In the Alps, it has been observed that the motion of Alpine rock glaciers has increased in the recent decades (see Bodin et al., 2009; Delaloye et al., 2008; Hartl et al., 2016; PERMOS, 2016; Springman et al., 2013). This acceleration has often been attributed to the temperature increase (Kääb et al., 2007). In turn, this temperature change affects the rheology of ice and is responsible for internal deformation of the rock glaciers. In addition, the change in the motion of the Alpine rock glaciers could also be explained by their liquid water content, associated with snow melting, rainy events (see Ikeda et al., 2008; Kenner et al., 2017) or permafrost melting. Large rock falls occurring at the roots of rock glaciers can contribute to their acceleration though their additional weight (Kummert et al., 2018). In all cases, the destabilization (e.g., Scotti et al., 2017) and, in some cases, the collapse of Alpine rock glaciers (e.g., Bodin et al., 2016) may represent a direct threat to infrastructures that need to be better understood and monitored (e.g., Arenson & Jakob, 2017; Haeberli, 1992; Schoeneich et al., 2011).

©2018. American Geophysical Union. All Rights Reserved.

Geophysics can bring complementary information to geomorphological studies in order to monitor the evolution of the distribution of material properties of rock glaciers (e.g., Hilbich et al., 2009; Kellerer-Pirklbauer & Kaufmann, 2017; Mewes et al., 2017; Springman et al., 2012). DC (direct current) resistivity has become an increasingly popular geophysical method for investigating the subsurface conditions in permafrost environments in loose deposit or rock slopes. This is because of the much lower conductivity of ice and permafrost with respect to unfrozen sediments and bedrock (see, for instance, Scott et al., 1990; Maurer & Hauck, 2007; Kneisel et al., 2008; Dafflon et al., 2013; Scapozza & Laigre, 2014; Supper et al., 2014; Dafflon et al., 2016). Electrical resistivity tomography (ERT) has been used to reveal detailed 2-D reconstructions of massive ice lens and ice-bearing layers (Hauck et al., 2003; Kneisel, 2004).

Rock glaciers are composed of materials in four different phases: two solid phases (rock/soil matrix and ice), liquid (unfrozen pore water with some ions), and air-filled pore space and cavities. The respective proportions of the various materials can be determined in laboratory analysis on sample cores obtained by drilling or camera inspection in boreholes (e.g., Arenson et al., 2002; Arenson & Springman, 2005). The composition of the rock glaciers can also be inferred through indirect geophysical investigations (see Hauck & Kneisel, 2008, and references herein for a review). That being said, ERT yields only qualitative information on the thermal state of materials because electrical conductivity depends on many parameters including water content, salinity, cation exchange capacity, and temperature. In addition, it is not sure that neglecting the effect of surface conduction (occurring at the liquid water/ice or solid interface) in the expression of the effective electrical conductivity of the mixture is a correct assumption. This assumption is however widely used in the literature without any critical analysis or corroboration through petrophysical investigations (e.g., Thompson et al., 2012). For instance, Hauck et al. (2011) developed a model that combines ERT and seismic *P* wave velocity and uses the parameters in Archie's law (Archie, 1942) and an extended Timur's equation (Timur, 1968) to gain insight into the porosity distribution. Daniels et al. (1976) and Wu et al. (2017) also used Archie's law without questioning the basic assumption regarding neglecting surface conductivity in low salinity environments. This assumption has been broadly used in the literature (e.g., Ping-Yu et al., 2017) but needs to be further tested for rock glaciers and other permafrost landforms.

Induced polarization (IP) is an electrical method that has never been used in the study of mountain permafrost and rock glaciers. IP investigates the ability of porous materials to store reversibly electrical charges under the application of a primary electrical field (Kemna et al., 2012; Weller et al., 2010; Weller & Slater, 2012). Recently, this method has been used in Arctic studies in a qualitative way (e.g., Dafflon et al., 2013; Doetsch et al., 2015). Wu et al. (2017) presented few experiments of complex conductivity of an Arctic saline permafrost soils during freeze and thaw. However, they have not connected the parameters of the in-phase and quadrature conductivities with a mechanistic model and assumed that surface conductivity could be neglected in the expression of the electrical conductivity of the rock ice mixture. This assumption will be demonstrated to be incorrect in this paper thanks to the information brought by the IP data. The interest of the IP method is to provide additional information beyond resistivity itself. For instance, the recently developed dynamic Stern layer model can be used to separate the surface from the bulk conductivity contributions using chargeability measurements (Revil, 2013).

Three-dimensional geophysical investigations are sparse in the field of periglacial geomorphology. Early works exist with graphically combined results from 2-D ERT surveys on 3-D diagrams (e.g., Scapozza & Laigre, 2014). Some recent studies dealt with the display of 3-D data set using multiple intersecting 2-D ERT lines ("quasi-3-D" approach) in a rock glacier, which enabled a horizontal mapping of resistivity variations (Emmert & Kneisel, 2017; Kneisel et al., 2014). However, no real 3-D tomography has ever been tested in such environment.

In the present study, we have collected a unique data set of 3-D electrical resistivity and IP data on a rock glacier site located on the skiing domain of Val Thorens (Vanoise massif, France). To our knowledge, this is the first case study of an Alpine rock glacier where the active layer has been disturbed by anthropic activity associated with both the implantation of the pylons and the creation of a ski run over the rock glacier. In addition to the field data, we performed laboratory measurements on a soil sample from the site to improve the interpretation of the field results and the effect of liquid water saturation and temperature on chargeability. To our knowledge this is the first study looking at investigating the role of surface conductivity and the usefulness of IP to study rock glaciers. The field and laboratory data are also confronted with the prediction of the dynamic

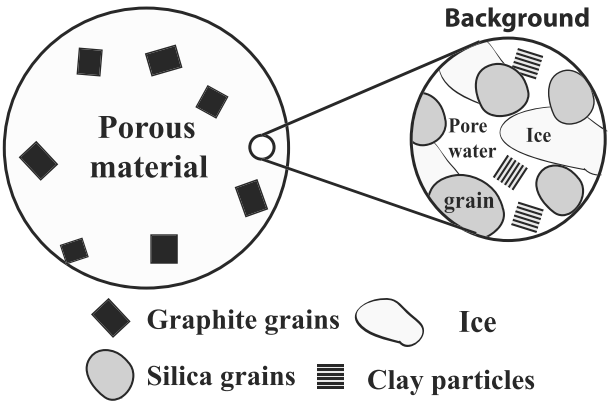

Figure 1. Type of composite used in the present study. The background material is made of the nonmetallic grains including ice and liquid pore water. It is polarizable. The chargeability of the mixture is increased by the presence of dispersed metallic particles made of graphite at our site. Our goal is first to describe the chargeability of such a complex mixture as a function of the chargeability of the background (mix of ice, pore liquid water, and nonmetallic grains) and the volume fraction of metallic particles.

Stern layer model developed and tested recently in a number of papers (Revil, 2013; Revil et al., 2017, 2018). Our end-goal is to answer three scientific questions: (i) Is IP capable of (and useful for) characterizing ground ice distribution in a rock glacier or mountain permafrost landforms? (ii) Can 3-D electrical conductivity and IP tomography be used to characterize the ground ice distribution on a degraded rock glacier? (iii) What is the influence of surface conductivity in the overall electrical conductivity of the rock ice mixture?

2. Background Theory

2.1. A Petrophysical Model

In this section, our primary goal is to summarize the results obtained recently to model the electrical conductivity and the chargeability of a mixture of minerals grains, liquid water, ice, and some metallic particles such as (often elongated) graphite particles, a semimetal present in some of the rocks at the field site investigated in this study (see Figure 1 for a general view of such complex mixture). Because of the polarization of the grains, the conductivity of rocks is dispersive, that is, it depends on the frequency. In the following, the quantity σ_∞ will denote the instantaneous conductivity, that is, the conductivity when all the charge carriers are mobile under the action of a primary electrical field (see Figures 2 and 3). This is the conductivity that is instantaneously measured in a porous material upon the injection of an electrical current (neglecting electromagnetic induction effects). In frequency-domain electrical conductivity measurements, σ_∞ is measured in the high-frequency range (at least 1 kHz or higher). At the opposite, the DC conductivity σ_0 denotes the conductivity of the material when some of the charge carriers have reached a certain pseudo-equilibrium state under the action of the primary (external or applied) electrical field or primary electrical current. In this case, concentration gradients have been fully established and when the primary current is shut down, these accumulated charges can go back to their initial equilibrium state by electro-diffusion (Seigel, 1959). In frequency-domain electrical conductivity measurements, the conductivity σ_0 denotes the low-frequency conductivity (typically determined below 0.1 Hz). The DC conductivity is smaller than the instantaneous conductivity because some electrical charges have lost their mobility and are now blocked by the process of polarization in and around the metallic particles. This process of polarization and concomitant loss of conductivity over time is illustrated in Figures 2 and 3.

The chargeability M (dimensionless) and the normalized chargeability M_n (S/m) can be defined in terms of the characteristic of the conductivity dispersion curve (see Mansoor & Slater, 2007; Seigel, 1959; and Slater & Glaser, 2003) as

$$M = \frac{\sigma_\infty - \sigma_0}{\sigma_\infty}, \tag{1}$$

$$M_n = \sigma_\infty - \sigma_0. \tag{2}$$

There are also other ways to determine the chargeability based on the secondary voltage decay after the shutdown of the primary current or using the relationships that can be established in some circumstances between the chargeability and the phase (Revil et al., 2017; Shuey & Johnson, 1973). The low-frequency polarization of rocks can find its root into the local accumulation of charges at the grain scale (see Figures 2 and 3 for nonmetallic and metallic particles, respectively, both components can be found in the mixture shown in Figure 1). For metallic particles, Revil, Florsch, and Mao (2015) and Revil, Abdel Aal, et al. (2015) have argued that the polarization takes place inside the metallic particles, while for nonmetallic particles, the polarization is controlled by the polarization of the electrical double layer around the grains (Revil, 2012, 2013).

We consider the general mixture shown in Figure 1. Based on the self-consistent approximation, Revil, Florsch, and Mao (2015) and Revil, Abdel Aal, et al. (2015) developed a complex conductivity model for metallic particles embedded into a porous matrix made of minerals and pore water. In this case, the chargeability M

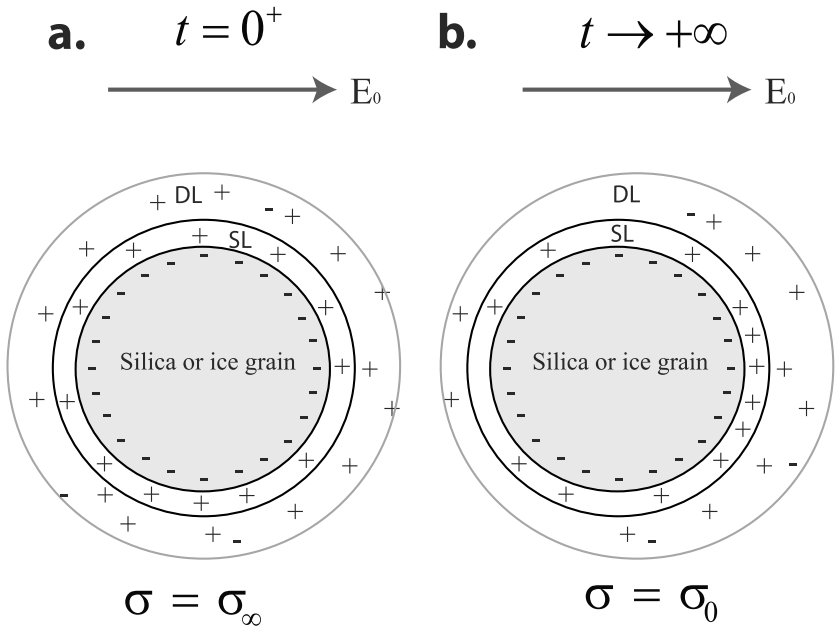

Figure 2. Polarization of a nonmetallic grain (e.g., belonging to the background material shown in Figure 1) coated by an electrical double layer. This electrical double layer is composed by a diffuse layer (DL) and a Stern layer (SL) of weakly adsorbed counterions that are mobile along the grain surface. (a) Just after the application of the primary electrical field $\mathbf{E}_0$, all the charge carriers are mobile (both in the pore water and in the electrical double layer). The instantaneous conductivity is σ_∞. (b) When the primary electrical field is applied for a long time, the conductivity is reduced to $\sigma_0 = \sigma_\infty(1 - M)$ where M stands for the chargeability of the material (dimensionless). Some of the charge carriers (those of the Stern layer) are now blocked at the edge of the grain in the direction of the electrical field. As a result, the conductivity of the material is reduced and therefore $\sigma_0 \leq \sigma_\infty$. The relaxation time would be the time for the charge carriers to go back to their equilibrium position when the primary electrical field would be shut down.

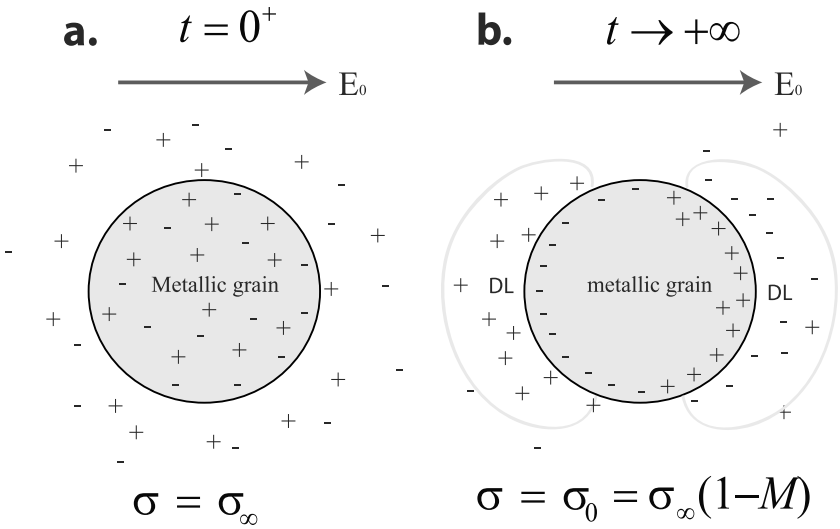

Figure 3. Polarization of a metallic grain. (a) We consider a metallic particle immersed into a nonpolarizable background material in which the charge carriers are ions. Just after the application of the external electrical field $\mathbf{E}_0$, all the charge carriers inside (electrons and p-holes) and outside (cations and anions) of the metallic particle are mobile providing the instantaneous conductivity σ_∞. The metallic particle appears highly conductive. (b) For a very long application of the external electrical field, the metallic particle is entirely polarized and appears as an insulator (i.e., the charge carriers are not mobile anymore). The generated surface charges are responsible for the formation of field-induced electrical diffuse layers (DLs) in the vicinity of the metallic particle creating also a second source of polarization. This situation defined the direct current conductivity of the material $\sigma_0 \leq \sigma_\infty$. The relaxation time would be the time for the charge carriers to go back to their equilibrium position when the primary electrical field would be shut down.

defined by equation (1) is directly related to the (dimensionless) volume content of metallic particles φ_m by (Revil, Abdel Aal, et al., 2015; Revil, Florsch, & Mao, 2015)

$$M \approx \frac{9}{2}\varphi_m + M_b, \tag{3}$$

where M_b (dimensionless) denotes the chargeability of the background material (nonmetallic grains, liquid water, and ice). According to equation (3), the chargeability of the mixture is simply the sum of two contributions, one associated with the volumetric content of metallic particles (and therefore independent of pore water saturation and temperature) and a second directly associated to the chargeability of the background porous rock. This second contribution is dependent on both the liquid water saturation and its salinity but independent of the temperature (Revil, Abdel Aal, et al., 2015; Revil, Florsch, & Mao, 2015).

The model developed by Revil, Florsch, and Mao (2015) and Revil, Abdel Aal, et al. (2015) can be used to provide expressions for the instantaneous and DC conductivities of the mixture shown in Figure 1. The instantaneous and the steady state conductivities are related to the instantaneous (σ_b^∞) and steady state (σ_b^0) conductivities of the background material (subscript b) according to (Revil, Abdel Aal, et al., 2015; Revil, Florsch, & Mao, 2015)

$$\sigma_\infty \approx \sigma_b^\infty (1 + 3\varphi_m), \tag{4}$$

$$\sigma_0 \approx \sigma_b^0 \left(1 - \frac{3}{2}\varphi_m\right). \tag{5}$$

Equations (4) and (5) show that the conductivity of the mixture is higher than the conductivity of the background at high frequency (for which the conductivity of the metallic particles is much higher than the conductivity of the background) and smaller at low frequencies (the metallic particles behave as insulators since there are completely polarized; see details in Revil, Florsch, and Mao, 2015, and Revil, Abdel Aal, et al., 2015). The transition between high and low frequencies depends on the relaxation times corresponding to the polarization of the metallic particles.

As mentioned above, the normalized chargeability is the difference between the instantaneous conductivity and the DC conductivity, that is, $M_n^b = \sigma_\infty^b - \sigma_0^b$. The chargeability of the background is defined as the ratio between the normalized chargeability of the background and the instantaneous conductivity of the background material:

$$M_b = \frac{M_n^b}{\sigma_\infty^b}, \tag{6}$$

where the quantities σ_∞^b and σ_0^b (in S/m) denote the instantaneous and DC conductivities of the background material, respectively. In order to go further, we need a model for the polarization of the nonmetallic grains shown in Figure 2. According to the dynamic Stern layer model developed by Revil (2012, 2013), the normalized chargeability and instantaneous conductivity of the background material can be written as (Revil et al., 2017)

$$M_n^b = \theta \rho_g \lambda \, \mathrm{CEC}, \tag{7}$$

$$\sigma_\infty^b = \theta^2 \sigma_w + \theta \rho_g B \, \mathrm{CEC}, \tag{8}$$

where θ (dimensionless) denotes the water content (product of the porosity by the saturation) of the liquid water phase, σ_w (in S/m) denotes the pore water conductivity, ρ_g is the grain density (in kg/m^3, typically ρ_g = 2,650 kg/m^3 for minerals in sedimentary rocks), and CEC denotes the cation exchange capacity (in C/kg) of the background. The CEC denotes the quantity of exchangeable cation on the surface of minerals. Note that that the ice/liquid water interface is also charged (Drzymala et al., 1999) and possesses therefore a CEC. During freezing, there is a decrease of the water content because the saturation of the liquid water phase is decreasing. From equations (7) and (8), this implies a strong reduction in the conductivity and normalized chargeability. The last term of equation (8) corresponds to the so-called surface conductivity. In equation (10), B (in m^2 V^{-1} s^{-1}) denotes the apparent mobility of the counterions for surface conduction

(Waxman & Smits, 1968) and λ (in $m^2\,V^{-1}\,s^{-1}$) denotes the apparent mobility of the counterions for the polarization associated with the quadrature conductivity. This quantity λ is close to the apparent mobility introduced by Vinegar and Waxman (1984) for the quadrature conductivity. We keep here the same notations for these parameters in the seminal papers of Waxman and Smits (1968) and Vinegar and Waxman (1984). More precisely, B includes the contribution of the mobility of the counterions in the Stern and diffuse layers affected by the fraction of counterions in each layer (see Revil et al., 2017, 2018, for a detailed discussion). The quantity λ denotes the contribution of the Stern layer to the overall mobility. This mobility is associated with the ions that will contribute to the polarization process and therefore that are not available anymore for the conduction process at low frequencies (Revil, 2013; Revil et al., 2017, 2018). In developing equations (7) and (8), we have assumed that the porosity and saturation exponents (m and n, respectively) are equal to 2 (see Revil et al., 2017, 2018, for a more complete model). From equations (6)–(8), the DC conductivity of the background material can be written as

$$\sigma_0^b = \theta^2\sigma_w + \theta\rho_g(B-\lambda)\,\mathrm{CEC}. \tag{9}$$

We introduce now the dimensionless number R given by $R = \lambda/B$, which will be of paramount importance in this paper to decide if surface conductivity dominates the bulk pore water contribution or not. This dimensionless number is fundamentally defined as the ratio between the normalized chargeability of the background $M_n^b = \theta\rho_g\lambda\,\mathrm{CEC}$ and the surface conductivity $\sigma_S = \theta\rho_g B\,\mathrm{CEC}$ (see Revil, 2013; Weller et al., 2013). Finally, an expression of the chargeability of the background material can be obtained using equations (6) to (8)

$$M_n^b = \frac{\rho_g\lambda\,\mathrm{CEC}}{\theta\sigma_w + \rho_g B\,\mathrm{CEC}}. \tag{10}$$

At low salinities, when surface conductivity dominates the pore water conductivity, we define the dimensionless Dukhin number as $\mathrm{Du} = \rho_g B\,\mathrm{CEC}/\sigma_w\theta$. It represents the ratio between the surface conductivity $\sigma_S = \theta\rho_g B\,\mathrm{CEC}$ to the bulk conductivity $\theta^2\sigma_w$. At low salinities (which is equivalent to $\mathrm{Du} >> 1$), we obtain the simplified result

$$\lim_{\mathrm{Du}>>1} M_n^b = \frac{\lambda}{B} = R. \tag{11}$$

This means that there is a universal value R for the limit of the chargeability of the background material shown in Figure 1 at low salinities whatever the temperature and saturation. In other words, if the chargeability is equal to the dimensionless number R, this means that surface conductivity dominates the bulk pore water conductivity and vice versa. This is one of the most important point that will be made in this paper. At low salinities and from equation (8), the conductivity of the material can be approximated by the expression of the surface conductivity and therefore, we have

$$\sigma_\infty^b \approx \theta\rho_g B\,\mathrm{CEC}. \tag{12}$$

At low salinity (i.e., $\mathrm{Du} >> 1$). We point out that equation (12) means that at low pore water salinity, the expression of the conductivity is not controlled by the conductivity of the pore water σ_w at the opposite of what is written in a number of publications. It is controlled by the water content, the CEC, and the temperature through the dependence of B with the temperature T. From equations (4) and (12), we can easily define an expression for the instantaneous conductivity of the mixture shown in Figure 1. Note however that small amounts of graphite may have a drastic impact on the chargeability but only a weak effect on the electrical conductivity itself so equation (12) represents always (to a good approximation) the conductivity of the mixture shown in Figure 1.

Recently, Revil et al. (2017) developed a large database for the complex conductivity of soil samples. This database can be used to prove the validity of the previous point. Figure 4 shows that at low salinities, the normalized chargeability is proportional to the conductivity of the soil samples and that the ratio between both is close to $R = 7 \times 10^{-2}$. This means that for these samples (characterized by high CEC because of their content in smectite), their conductivity (at low salinities) is dominated by their surface conductivity.

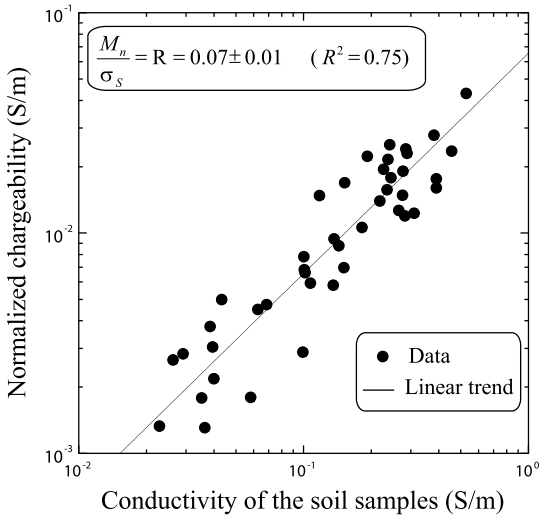

Figure 4. Linear relationship between normalized chargeability (between 0.1 Hz and 40 kHz) and surface conductivity for the soil samples at a low salinity corresponding to a pore water conductivity of 0.03 S/m (NaCl, 25 °C). The normalized chargeability M_n (expressed in S/m) is defined as the difference between the in-phase conductivity at high and low frequencies: $M_n = M\sigma_\infty = \sigma_\infty - \sigma_0$. The plain line corresponds to the best fit of the data using a linear model between the normalized chargeability and the surface conductivity. The value of the slope is equal to the value of the dimensionless number R. Data from Revil et al. (2017).

Another test is provided in Figure 5 where we display the chargeability of sands, sandstones, and soils as a function of their CEC. All the measurements are reported here at very low salinity at which surface conductivity dominates the bulk electrical conductivity. As predicted by equation (11), the chargeability is independent of the CEC and equal to the dimensionless number $R = 8 \times 10^{-2}$ (independent of temperature and saturation). While not show here (see Revil et al., 2017, for further details), when the chargeability is equal to R, the conductivity data become independent of the pore water conductivity at these low pore water salinities, which, in other words, means that the conductivity is controlled by the surface conductivity.

In the previous modeling effort, the effect of the ice itself has been accounted for only through its effect on saturation (water content θ) on the expression of the normalized chargeability of the mixture shown in Figure 1. That being said, ice grains can also polarize because of ionic and Bjerrum defects in the ice crystals themselves (Bjerrum, 1952). We will keep this point in mind when analyzing the laboratory data in section 5 when the Bjerrum polarization will show up in the complex conductivity data obtained in the laboratory. A complete analysis of this polarization mechanism will stay, however, outside the scope of the present paper.

2.2. Time-Domain IP

IP can be performed either in time-domain (TDIP) or in frequency domain, the latter method being often called *spectral IP* (*SIP*) when multiple frequencies are used. SIP is often performed in the laboratory, while TDIP is usually used in the field because most resistivity meters can easily perform such measurements. This is exactly what has been done in this work for the field data. This is why, in this section, we describe in more details time domain IP data.

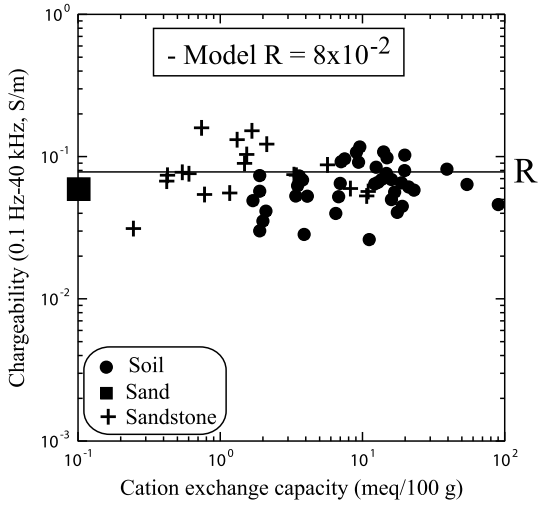

Figure 5. Chargeability (determined between the frequency range 0.1 Hz and 40 kHz) versus CEC (cation exchange capacity) for the background material at low salinities. The CEC measurements have been performed with the cobalthexamine method. The sandstone data are from Vinegar and Waxman (1984; all samples at the lowest salinity, the normalized chargeability are obtained using quadrature conductivity data at a pore water conductivity at 0.1 S/m NaCl, 25 °C), and the soil data are from Revil et al. (2017) and measured at a pore water conductivity of 0.03 S/m (NaCl, 25 °C).

In TDIP, a bipolar periodic square current waveform is used to inject the primary current in the ground (Figure 6a). Great care needs to be also taken in separating the current and voltage cables (Figure 6b). The flow of this primary current is responsible for the polarization of the grains (Figures 2 and 3). The polarization of the grains is synonymous of charge accumulations at some polarization length scales. The formation of these charge accumulations means that the drift of the charges is controlled by electrochemical potentials, and therefore, a secondary current density of electrochemical nature is also generated in the ground. In turn, this secondary current density is generating a secondary electrical field. Seigel (1959) was the first to correctly identify this correspondence between the underlying process and the different parameters defined in the time and frequency domains polarization to represent the polarization process.

Coming back to the description of TDIP, the secondary voltage curve is measured after the shutdown of the primary current between the electrodes M and N. This secondary voltage corresponds to the component of the secondary electrical field in the MN direction. Using these voltage values, one can derive the partial apparent chargeability in each window W_i during the decay of the secondary voltage over time (Figure 6). Indeed, during the decay of the secondary voltage $\psi(t)$, and considering two times t_1 and $t_2 > 0$ ($t = 0$ corresponds to the shutdown of the primary current), the measured partial chargeability is defined as

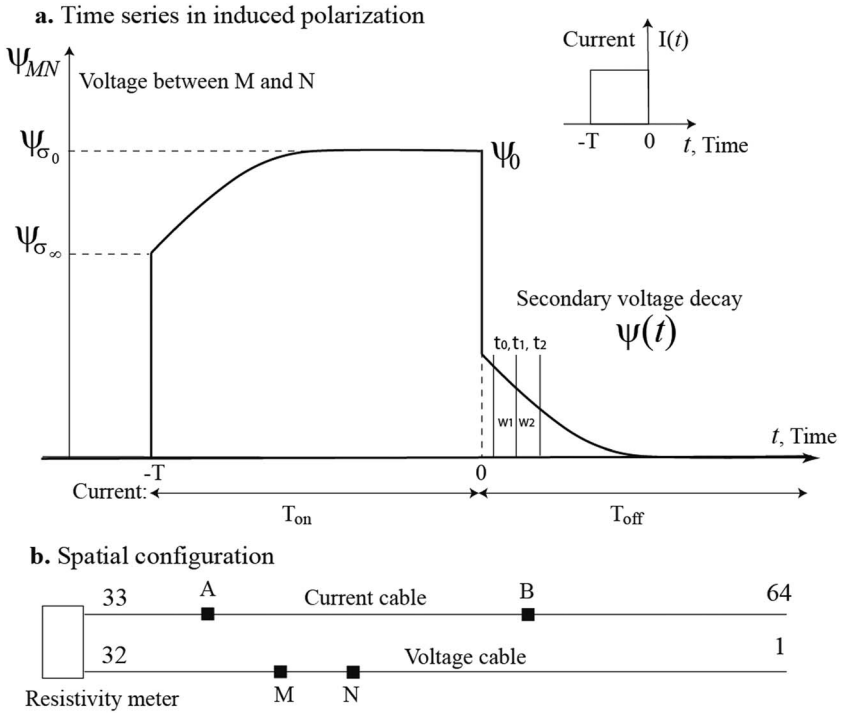

Figure 6. Time-domain induced polarization measurements. (a) Measured potential difference between two voltage electrodes M and N for a box current input (through current electrodes A and B). The decaying secondary voltage (for $t > 0$) is decomposed into windows (W_1, W_2, etc.) separated by characteristic times (t_0, t_1, t_2, …). The partial chargeabilities are determined for each of these windows. (b) Electrode configuration for the induced polarization measurements. We separated the current cable form the voltage cable. In other words, all the current electrodes are located on one cable while all the voltage electrodes are located on the second cable. The two cables are separated by a distance of 1 m to minimize electromagnetic couplings between the wire. This configuration is also made to avoid the effect of the polarization of the electrodes on the measurements. The numbers refer to the electrode number in the protocol fie from 1 to 64.

$$M_{t_1,t_2} = \frac{1}{\psi_0}\int_{t_1}^{t_2}\psi(t)dt \quad , \tag{13}$$

where ψ_0 denotes the difference of potential between the electrodes M and N just before the shutdown of the primary current and $\psi(t)$ denotes the secondary voltage decaying curve between electrodes M and N (Figure 6). The partial chargeability and the chargeability are related to each other by $M_{t_1,t_2} \approx M(t_2 - t_1)$ as long as the two times t_1 and t_2 are chosen such as $t_1 < t_2 \ll \tau$ where τ denotes the main relaxation time of the material for IP (Florsch et al., 2010).

2.3. Conductivity and Chargeability Tomography

As widely described in the literature, the classical approach to invert TDIP data in terms of chargeability is to apply the method proposed by Seigel (1959). In this approach, the polarization effect is treated as a perturbation of the subsurface electrical conductivity. As mentioned above, the DC conductivity σ_0 is related to the instantaneous conductivity σ_∞ by $\sigma_0 = (1 - M)\sigma_\infty$. The inversion of the secondary voltage decaying function can then be treated with a two-step procedure. In the first step, the inversion of the instantaneous conductivity σ_∞ is performed without polarization effect. In the second step, an inversion of the chargeability is carried out using the conductivity distribution obtained in the first step.

Because the frequency of the bipolar periodic transmitter waveform is low enough, the quasi-static approximation of the Maxwell's equations can be used neglecting induction. The scalar potential ψ_{σ_∞} (in V) is introduced to ease the calculation of the Maxwell's equations in this situation (Figure 6a). The governing equations are formed by the Poisson's equation as

$$\nabla\cdot\left(\sigma_\infty\nabla\psi_{\sigma_\infty}\right) = -I\delta(\mathbf{r}-\mathbf{r}_s) \ , \tag{14}$$

with the following boundary conditions at the Earth's surface:

$$\frac{\partial\psi_{\sigma_\infty}}{\partial\hat{n}} = 0, \tag{15}$$

(i.e., the normal component of the electrical field vanishes at the ground surface). In these equations, $\hat{n}$ denotes the unit normal vector to ground surface, I is the injected current (in A), and $\delta(\mathbf{r}-\mathbf{r}_s)$ (m^{-3}) denotes the 3-D delta function where $\mathbf{r}$ and $\mathbf{r}_s$ (in m) are the vector position and the position vector of the current source, respectively (I positive for current injection and negative for current withdrawal from the ground). The potential is taken equal to zero at the other boundaries placed far away from the domain of interest to mimic infinity.

Tomography is obtained by looking for the model vector $\mathbf{m}^*$ minimizing the following objective function $\mathbf{P}^\lambda(\mathbf{m})$:

$$\mathbf{P}^\lambda(\mathbf{m}) = \|\mathbf{W}_d(\mathbf{d}(\mathbf{m})-\mathbf{d}_{\text{obs}})\|^2 + \lambda\|\mathbf{W}_m\mathbf{m}\|^2 \ , \tag{16}$$

where the N-vector $\mathbf{m}$ is the model vector corresponding to the logarithm of the conductivity of each cell, the M-vectors $\mathbf{d}(\mathbf{m})$ denotes the predicted data for a model vector $\mathbf{m}$, the M-vector $\mathbf{d}_{\text{obs}}$ denotes the observed apparent resistivity data or chargeability, and λ is the regularization parameter that balances the data misfit (first term of the right-hand side of equation (16)) and the regularizer (last term of equation (16)). Usually, we have $M << N$ and the problem is underdetermined. The $M \times M$ matrix $\mathbf{W}_d$ is related to the data covariance matrix that is generated from the measured standard deviations on the measurements. In our study, the matrix $\mathbf{W}_m$ is considered to be the first-order gradient $N \times N$ matrix. Minimizing the objective function with respect to the model vector, we obtain the following iterative solution for the model vector

$$\mathbf{m}_{k+1} = \mathbf{m}_k + \delta\mathbf{m}_k, \tag{17}$$

where the perturbation of the model vector is given in the model space by

$$\delta\mathbf{m}_k = -\left[\mathbf{J}^T\left(\mathbf{W}_d^T\mathbf{W}_d\right)\mathbf{J} + \lambda\mathbf{W}_m^T\mathbf{W}_m\right]^{-1}\left[\mathbf{J}^T\left(\mathbf{W}_d^T\mathbf{W}_d\right)(\mathbf{d}(\mathbf{m}_k)-\mathbf{d}_{obs}) + \lambda\mathbf{W}_m^T\mathbf{W}_m\mathbf{m}_k\right] \ . \tag{18}$$

where $\mathbf{J}$ is the sensitivity matrix and $\mathbf{A}^T$ denotes the transpose of the matrix $\mathbf{A}$ ($\mathbf{A}$ being a general matrix). Convergence is reached when the perturbation model vector is smaller than a given threshold. Since calculating the sensitivity matrix is the most time-intensive part in the optimization, we use the reciprocity method to calculate the first sensitivity matrix and then update the sensitivity matrix using Broyden's method at each iteration (Broyden, 1965).

Equation (14) can be used to rerun the forward modeling step for DC conditions, and the potential distribution ψ_{σ_0} is obtained. The apparent chargeability M_a is defined as

$$M_a = \frac{\psi_{\sigma_\infty} - \psi_{\sigma_0}}{\psi_{\sigma_\infty}} \ . \tag{19}$$

During the inversion, M_a in equation (21) is treated as the computed apparent chargeability. In practice, we only assemble the conductivity sensitivity matrix, then the chargeability matrix is deduced from it after some mathematical derivation, as follows:

$$\frac{\partial d_i}{\partial \log M_j} = -\frac{M_j}{1-M_j}\frac{\psi_{\sigma|i}}{\left(\psi_{M|i}\right)^2}\frac{\partial\psi_{M|i}}{\partial\log\sigma_j} \ , \tag{20}$$

in which, $\partial d_i/\partial \log M_j$ denotes the chargeability sensitivity matrix and $\partial\Psi_{M\ |\ i}/\partial \log \sigma^j$ is the conductivity matrix associated to $\sigma_0 = \sigma_\infty(1-M)$. This approach will be used for computing the 3-D distributions of the electric conductivity and chargeability in the field case study discussed below. Benchmark of the

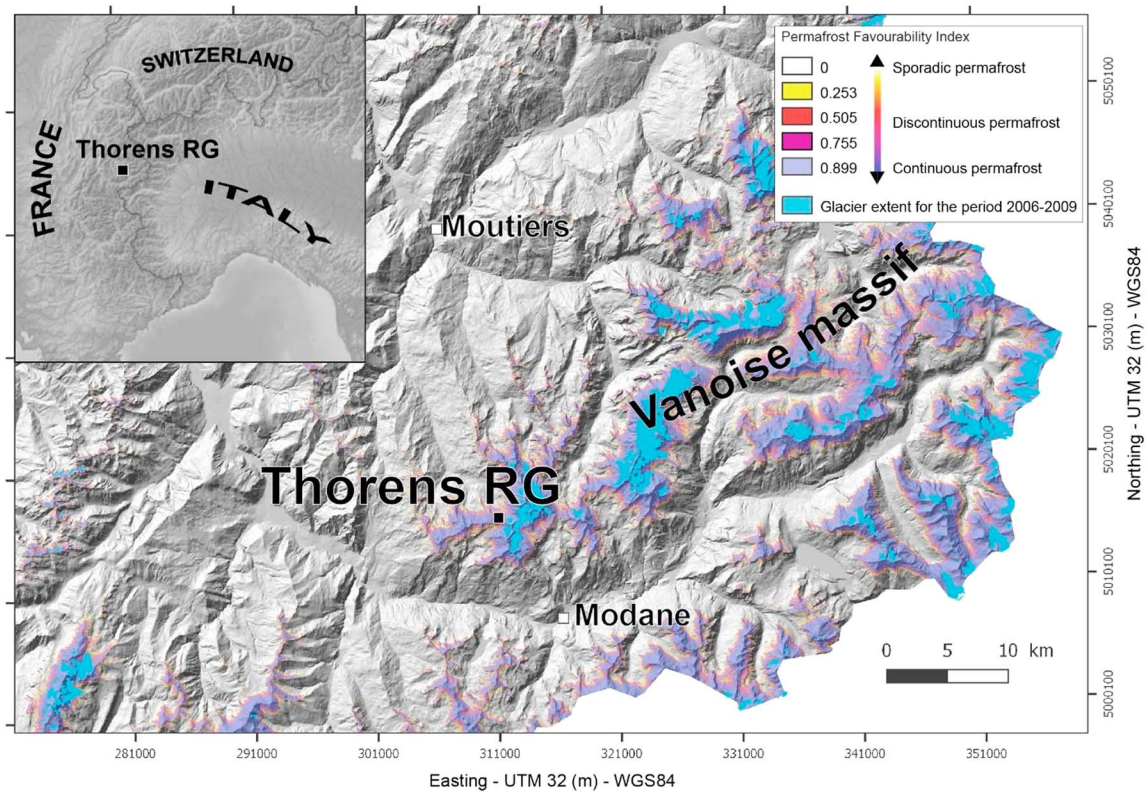

Figure 7. Localization of the Thorens rock glacier (RG) in the Vanoise massif (IGN 25-m digital elevation map with glacier extent for the period 2006–2009 from Gardent et al., 2014). The potential permafrost distribution in the French Alps (source: Marcer et al., 2017) is also shown.

method on synthetic and true field data has already been performed in Soueid Ahmed, Revil, Jardani, et al. (2018) and Soueid Ahmed, Revil, Byrdina, et al. (2018) for the resistivity and chargeability problems and by Qi et al. (2018).

3. Geophysical Surveys

3.1. Site Location and Description

We focus our attention on a small portion of the Thorens rock glacier located in Val Thorens ski resort (Vanoise massif, France), on a North-oriented slope between 2,800 and 2,950 masl (meters above sea level, Figure 7). This rock glacier is shaped by two tongues of approximately 60 × 250 m composed of debris materials from sedimentary rocks (sandstone and shale with clay of Houiller with graphite, see Guillot, 1982; Debelmas, 1989). The rocky ridge to the East dips almost under the right lobe of the rock glacier, probably forming a natural dam to the water flow and the rock glacier. Due to the rock glacier and this rocky ridge, a temporary lake is present immediately East of the rock glacier with a likely resurgence between the rock glacier and the bedrock (Figures 8 and 9). The permafrost favorability index map (Marcer et al., 2017) describes the present spatial distribution of permafrost in the French Alps. In the investigated area, the permafrost favorability index is equal to 0.95, which means that ice-rich permafrost in the rock glacier is expected in all conditions. The occurrence of ice-rich permafrost in the rock glacier was also reported by geotechnical studies in 2008 and 2010 from two 2-D ERT profiles (Fabre et al., 2015). In the same way, the potentially thawing permafrost map (Marcer et al., 2018) proposes a spatial distribution of the degraded permafrost in the French Alps. For the studied site, this map indicates a potentially thawing permafrost of 0.98, which means the whole rock glacier is localized in a "permafrost zone undergoing significant degradation" caused by an increase in the mean annual temperature of the air. These studies helped in designing the foundations of the Funitel cable car with recommending an offset layout upstream of the rock glacier front. The engineering

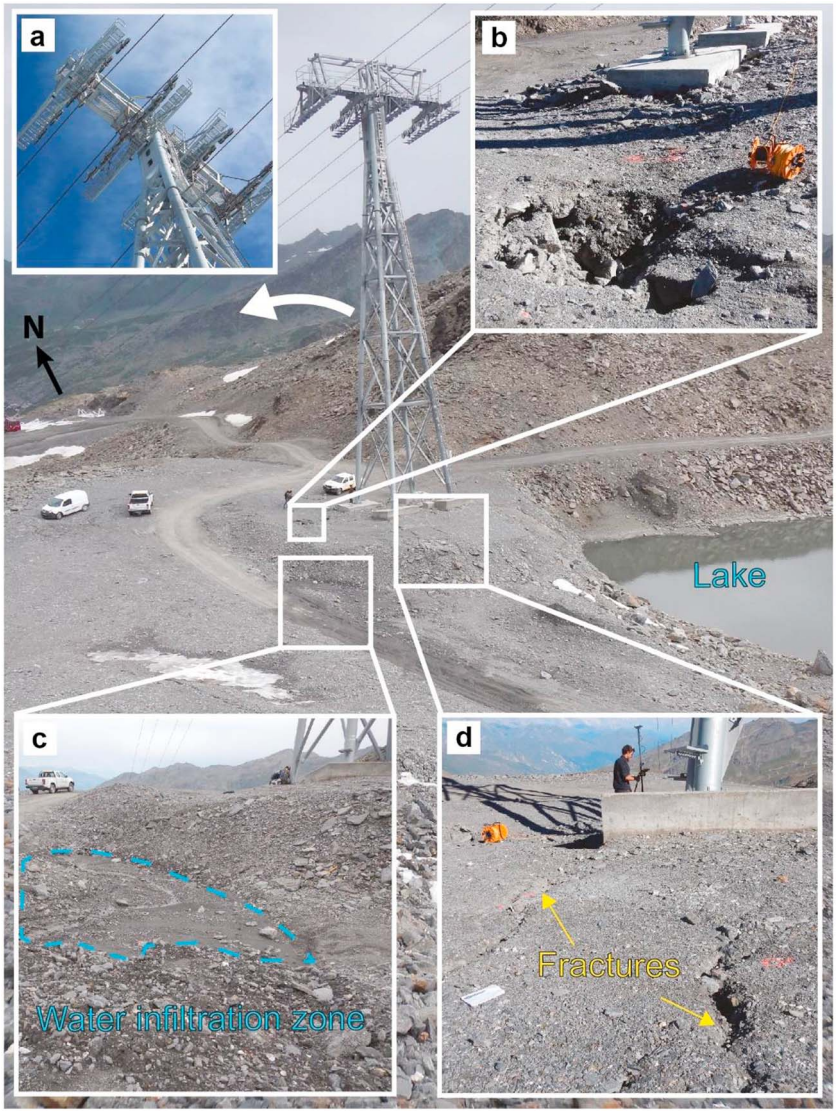

Figure 8. Illustration and destabilization signs in the vicinity of Pylon #2 of the Funitel of Thorens. (a) Offset at the top of the pylon between the cable and the pendulum. (b) Metric subsidence west of the foundations. (c) Water infiltration zone, upstream of the pylon platform. (d) Subsurface fractures visible upstream of the foundations.

company who designed the Funitel had planned a possible adaptation of the pylon in the direction of the slope on an adjustable rail, in case of glacier movement.

The Funitel was built during the summer 2011. It is composed of four pylons among which three were potentially set up on or in the vicinity of permafrost (Duvillard et al., 2015). Pylon 2 was built on in the vicinity of the right lobe of the rock glacier after performing a geotechnical study (Fabre et al., 2015). A ski run was built on the rock glacier itself after an earthwork of the superficial layer (Figures 8 and 9). Afterward, a movement started to happen between its implantation in 2011 until July 2016 with a cumulative displacement of the foundations of pylon of 2 to 25 cm laterally and 55 cm vertically (Figure 8). This occurred in the western foundations of the pylon. This displacement was likely associated with the occurrence of some subsidence and thermokarsts nearby (Figure 8). These movements generated a horizontal shift of approximately 1.5 m at the top of Pylon 2. During the summer 2017, Pylon 2 was anchored deep into the bedrock using over 20 steel struts. Each steel strut has a length of 20 m. However this amount of metal remains small to generate any spurious IP anomaly at the position of the pylon because of the electrode separation (5 m) in our surveys. Indeed, the volumetric amount of metal remains smaller than 1% even for the measurements performed

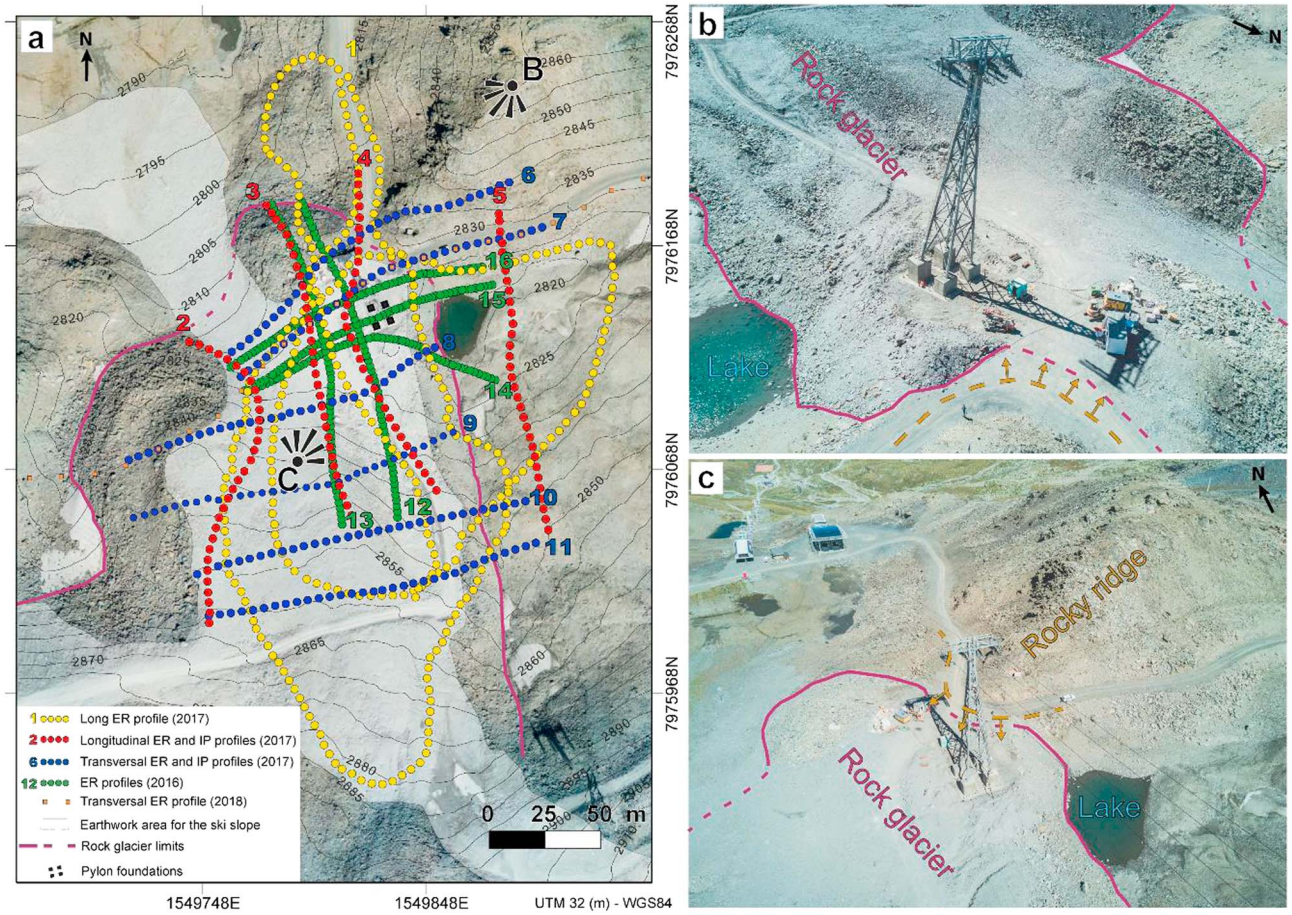

Figure 9. Map and photography of the test site with the Thorens rock glacier. The picture shows the location of the ski run and approximate location of the rock glacier (prior the geophysical study). The locations of the resistivity and induced polarization profiles are also shown. (a) Position of the electrical resistivity (ER) and induced polarization (IP) profiles acquired with the multigradient and Wenner arrays. (b) View of Pylon #2. (c) Another view of Pylon #2, the rocky ridge (rich in graphite), the lake, and the rock glacier prior the geophysical study.

in the vicinity of the pylon (see Revil, Abdel Aal, et al., 2015 and Revil, Florsch, and Mao, 2015 for a theory accounting for the presence of metallic bodies).

3.2. Electrical Resistivity and IP Surveys

ERT and IP geophysical field campaigns were carried out in September 2016 and July 2017 with a total of 16 ERT profiles and 10 IP profiles (see Table 1 and Figure 9) using the Wenner and the multigradient arrays. All the electrodes were stainless steel rods. Profiles 1, 12, 13, 14, 15, and 16 were only used for acquiring ERT data. The measurements were carried out using an ABEM SAS4000 (four-channel resistivity meter). A total of 4,798 resistances and 2,900 apparent chargeabilities were performed. Electrode coordinates were obtained using a

Table 1
Details on Electrical Resistivity and Induced Polarization Surveys

Profile	Date of survey	Number of 2-D profiles collected	Electrode array type	Electrode spacing (m)	Number of electrodes	Number of data points
ER2016	1–2 September	5	Wenner 64	2 and 2.5	320	2,004
ER2017	24–27 July	11	Wenner 32	5	635	2,799
IP2017	24–27 July	10	Grip32	5	315	2,021
ER2018	27–28 August	1	Wenner 32	20	32	144

Note. The Grip32 is a mutigradient array for 32 electrodes. ER2016 and ER2018 denote the electrical resistivity profiles performed in 2016 and 2018, while ER2017 and IP2017 denote the electrical resistivity and induced polarization profiles performed in 2017. A long profile (ER2018) was also performed in 2018 (see Figure 10).

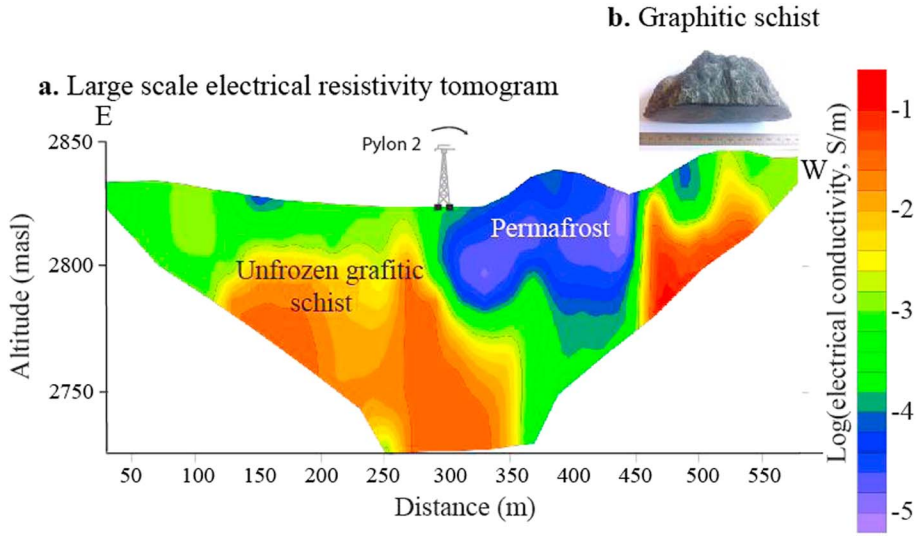

Figure 10. Large-scale electrical conductivity tomogram crossing the area of interest and picture of the dominant rock, a graphitic black schist. (a) Electrical conductivity tomogram showing the position of Pylon 2. The depth of the permafrost is roughly 50 m. The movement of the pylon seems related to the ongoing degradation of ground ice (and hence subsidence) following construction works of the pylon and earthworks for the ski run. Permafrost degradation is still ongoing with the possibility that there is still some residual ice existing around the pylon. Under conditions of permafrost degradation it is usually expected that unfrozen/liquid water and ice coexist at temperatures around −1 °C at this altitude. (b) Picture of a graphitic schist forming the main formation in this area.

real-time kinematic Global Positioning System (Trimble Geo7X) with a 2-cm accuracy. Electrode elevations were recovered using a linear interpolation scheme and a 1-m-resolution digital elevation model (DEM). This DEM was obtained using an unmanned aerial vehicle photogrammetry survey performed in August 2017 just after the acquisition of the geophysical data. An additional large-scale profile was done with 32 electrodes and an electrode spacing of 20 m (see Figure 10). It shows that the depth of the permafrost in around 50 m.

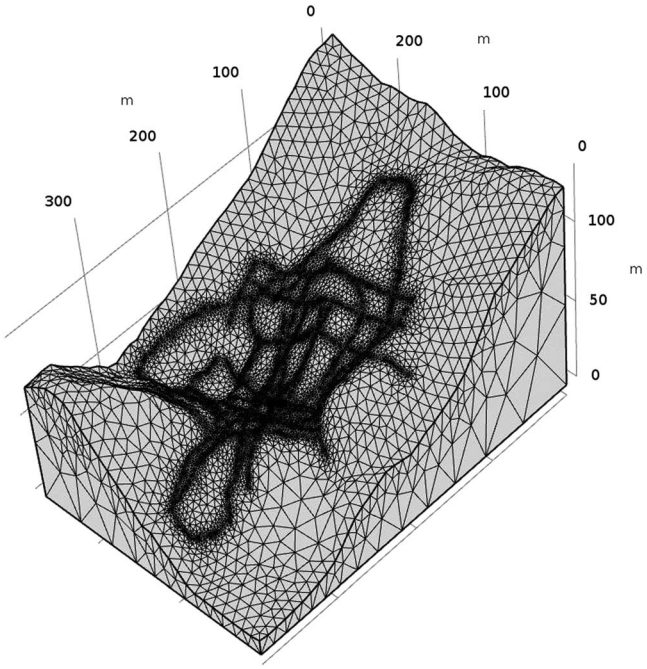

Figure 11. Mesh used for the finite element forward modeling of the electrical conductivity and induced polarization modeling. The mesh is refined close to the position of the electrodes and contains a total 48,839 elements. The same mesh is used for the forward and inverse modeling.

The forward and inverse modeling of the geophysical data was performed with the unstructured mesh shown in Figure 11 using the topography from the DEM. The domain of simulation was discretized into 48,839 elements with the same mesh used for the forward and inverse modeling. The IP profiles (i.e., Profiles 2 to 11) use the gradient configuration for the collection of the apparent chargeability while we used gradient and Wenner-alpha arrays for the resistivity. The choice of the gradient configuration for the IP array is motivated by the fact that we separated the cables for the current injection from the cables used for the voltage measurements (see Dahlin et al., 2002). This was done in order to reduce the electromagnetic coupling effects especially between the wires contained in the same cable (there are 32 wires in the same cable with the equipment we used). In other words, the electrodes used for injecting the current are different from those used for measuring the induced voltages. This method is used for acquiring high quality time-domain IP data as discussed below. The period for the current injection was 1 s and the secondary voltage was followed during a time window of 1.5 s (the partial chargeabilities were determined using 10 windows of 100 ms, and a dead time of 50 ms was used). We performed up to eight stacks for the resistivity measurements and two stacks for the IP measurements. These stacks were used to evaluate the data covariance matrix considered to be a diagonal matrix in this study.

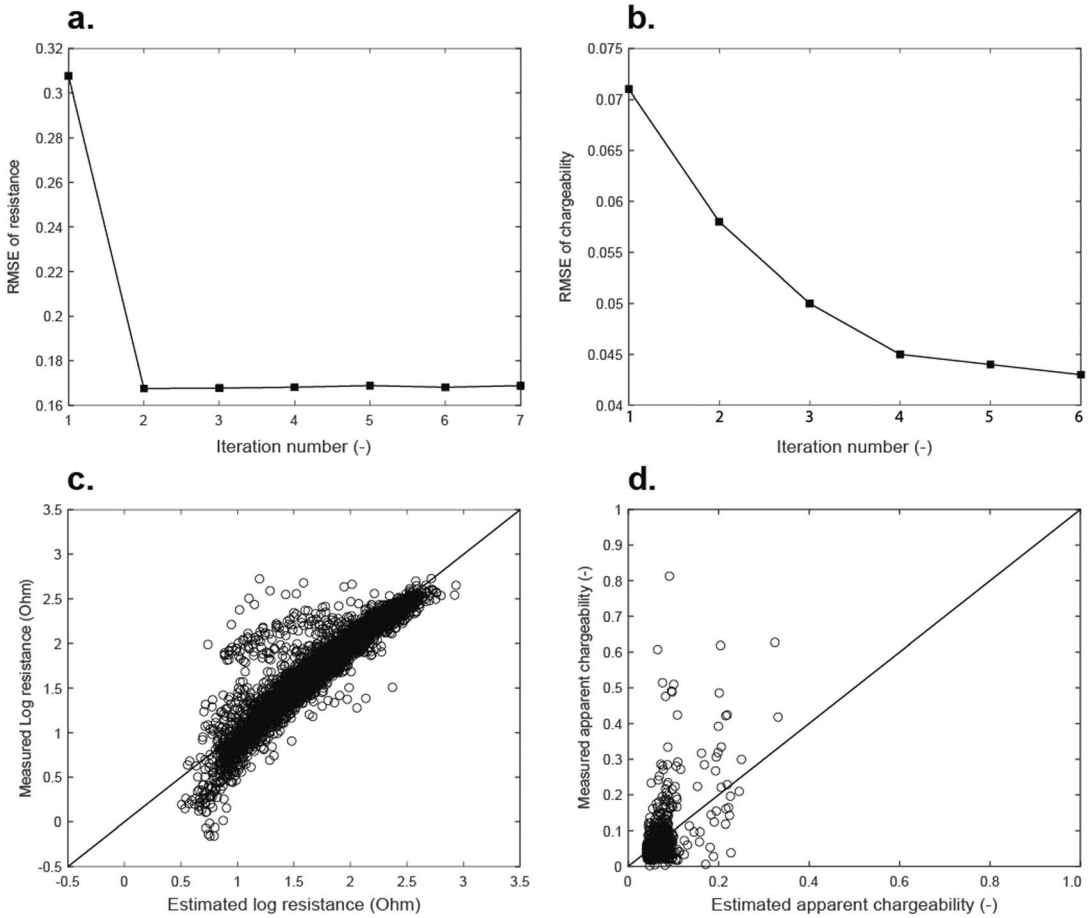

Figure 12. Convergence and data fit. (a) RMS error of the data misfit function for the apparent resistivities. (b) RMS error of the data misfit function for the apparent chargeabilities. (c) Measured versus estimated observed resistances. (d) Measured versus estimated apparent chargeabilities. Note that the apparent chargeabilities are clustered around the value of $R = 0.08$ indicating a very homogeneous tomogram for the chargeability and ipse facto that surface conductivity dominates the overall conductivity response.

As the intrinsic conductivity and chargeability are positive quantities, we inverted the decimal logarithms of these values avoiding the appearance of negative values in the tomograms. The convergence of the inversion process was reached when two consecutive iterations induced a change of the objective function smaller than 0.001 (defining here the convergence criterion, Figure 12). In our case, convergence was reached after five iterations for the electrical conductivity and eight iterations for the chargeability.

4. Results

4.1. Conductivity and Normalized Chargeability Tomography

The convergence and data fit are shown in Figure 12. The 3-D electrical conductivity tomogram is shown in Figure 13. The rock ice mixture is typically comprised between 10^{-4} and 10^{-5} S/m. In contrast, the unfrozen portion of the ground has a conductivity in the range 10^{-2} to 10^{-3} S/m. The in situ electrical conductivity of the pore water in the unfrozen portion of the site is ~0.01 S/m (at 25 °C), so the pore water is poorly mineralized. The 3-D normalized chargeability tomogram is shown in Figure 14. The rock ice mixture is located on the frozen side of the investigated area and is characterized by very low normalized chargeability values associated with the presence of ice. It is possible to distinguish the rock glacier and bedrock layers near the pylon due to high sensitivity of the tomograms in this area. The contrast is less clear in the upper part of the rock glacier.

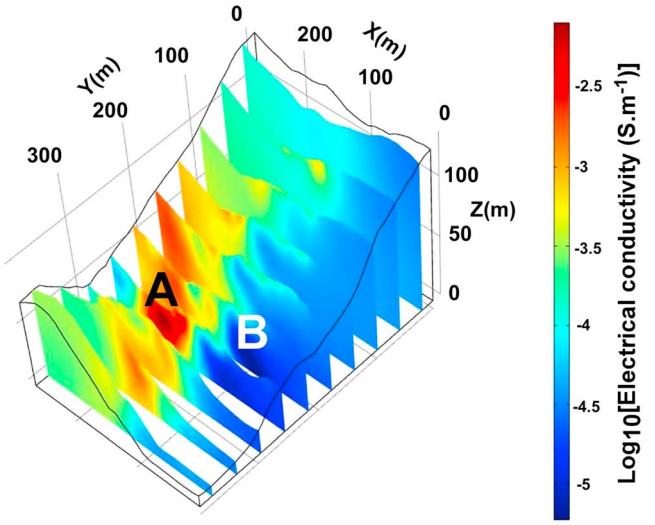

Figure 13. Three-dimensional electrical conductivity tomogram showing that the domain area is grossly divided into two compartments. The ice rock mixture is typically comprised between 10^{-4} and 10^{-5} S/m, while the water-saturated compartment is characterized by a much higher electrical conductivity. Compartments A and B correspond to the unfrozen and frozen areas, respectively.

Figure 15 displays the 3-D chargeability distribution. We have seen in section 2 that the chargeability cannot be higher than 8×10^{-2} except in the presence of metallic particles such as graphite present in the graphitic schist shown in Figure 10b. The presence of graphite is therefore revealed in an area where we see on the surface carboniferous rocks outcropping. Figure 16 shows typical partial chargeability decay curves. They first evidence the high quality of the IP data. While in this paper we are not interested by the characteristic relaxation time for IP, we see clearly that in the rock glacier area the relaxation time is much smaller than in the unfrozen area. This is an expected result since the relaxation time is expected to be temperature dependent. In future contributions, it will be interesting to image the relaxation time using IP data, which we cannot do at this point.

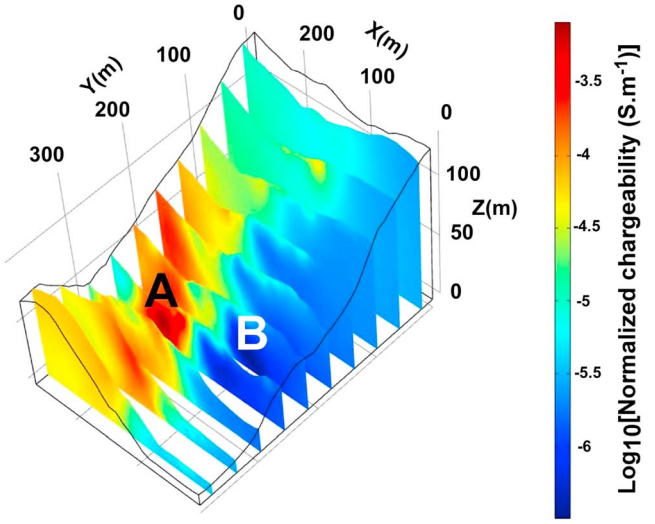

Figure 14. Three-dimensional normalized chargeability tomogram. The rock glacier is located on the right side and is characterized by very low normalized chargeability values ($<10^{-5}$ S/m) associated with the presence of the rock ice mixture. Compartments A and B correspond to the unfrozen and frozen areas, respectively.

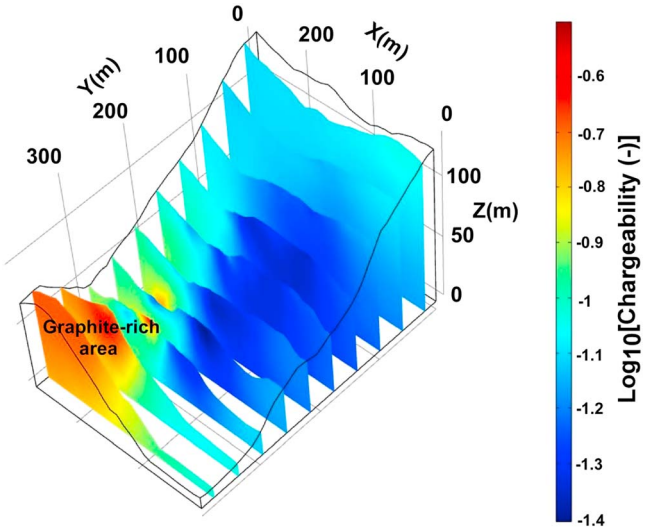

Figure 15. Three-dimensional chargeability tomogram. In absence of metallic particles, the chargeability cannot be higher than 8×10^{-2}. Values typically above 8×10^{-2} are associated with areas that contain graphite. The graphite-rich area is shown on the tomogram.

4.2. Interpretation

Two-dimensional cross sections are extracted from the 3-D ERT and IP tomograms and shown in Figures 17–19 with the final interpretation shown in Figure 20. These tomograms indicate the following points: (i) The conductivity of the rock ice (in the range 10^{-4} to 10^{-5} S/m) seem to correspond to a "temperate" permafrost, that is, close to the melting temperature with a high liquid water content (Hauck & Kneisel, 2008). Note, however, that the conductivity of a rock ice mixture is also a function of the respective fractions of rock and ice and the conductivity of the rock. A low conductivity may therefore also indicate comparatively low ice contents and/or comparatively high conductivity of the host rock because of the presence of clay minerals. (ii) The pylon is located in an area without permafrost. It is close to a small lake located in an area where no permafrost is shown in the tomograms. The lake closed by the rocky ridge and rock glacier, induce

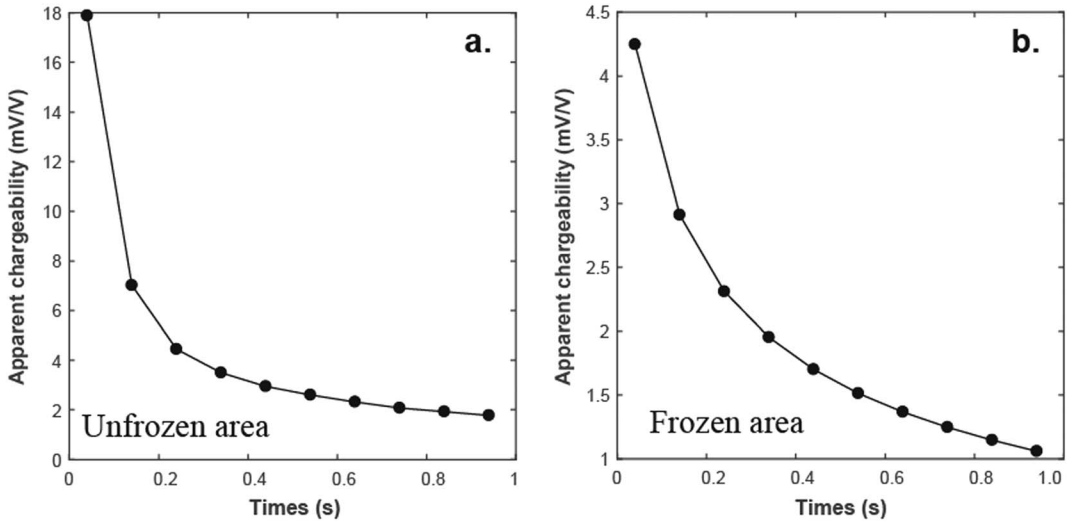

Figure 16. Secondary voltage decay (normalized by the primary voltage) as a function of time. The secondary voltage is used in mV, while the primary voltage is considered in volts, which explains the unit of m*V*/V. (a) First bipole in the liquid water-saturated zone. (b) Second bipole in the rock ice mixture (frozen) area. The relaxation time in the frozen area (τ = 0.22 s) is much longer than in the unfrozen area (τ = 0.09 s).

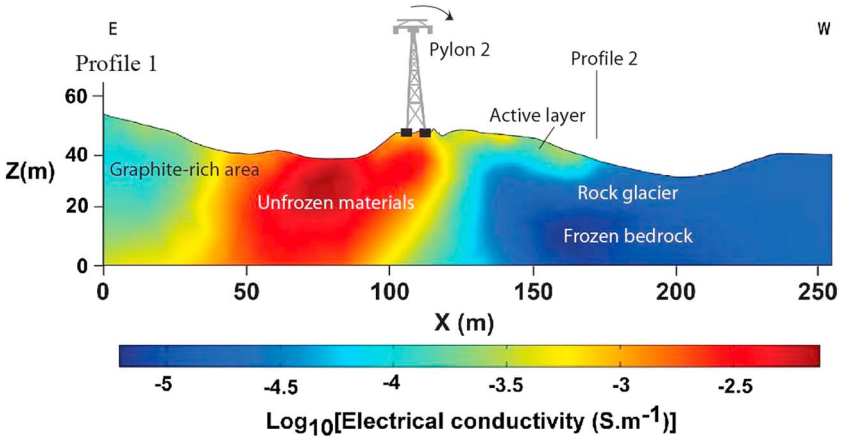

Figure 17. Two-dimensional cross section of electrical conductivity (Profile 1) extracted from the 3-D tomogram with the position of Pylon 2 in the vicinity of the interface between the resistive rock glacier and the conductive unfrozen ground. The conductivity rock glacier is typically comprised between 10^{-4} and 10^{-5} S/m. We also show the direction of the movement of the pylon.

probably a summer seasonally thawed area, allowing to keep the right part of the East lobe of the rock glacier with no permafrost (Kenner et al., 2017; Luethi et al., 2017; Figures 17–20). (iii) There is a deepening of the active layer thickness near the pylon, probably due to major earthwork associated with the recent creation of the platform for the pylon and the ski slope in 2011. In addition, the rock glacier displaces and reorganizes coarse materials from the surface layer.

There is some permafrost in the vicinity of the pylon. Its degradation has lead to deepening of the active layer and subsidence, which is causing the destabilization of the pylon. Figure 21 shows a 2-D cross section normal to the 2-D section described above. This new cross section is entirely localized on the rock glacier and so we use a scale more adapted to the rock glacier. The rock glacier is typically in the range $10^{-3.5}$ to $10^{-4.5}$ S/m while the bedrock appears much less conductive with a conductivity below 10^{-6} S/m. We observe a clear active layer of up to 10-m thickness, which might be related to ongoing degradation associated with the earthworks for the ski run at its surface.

In Figure 22, we plot, for all cells, the normalized chargeability versus the conductivity of the material (the ratio of both being the chargeability). With the exception of the data located close to the graphite-rich rocks, we see clearly that the data form a linear trend that is consistent with the soil data of Revil et al.

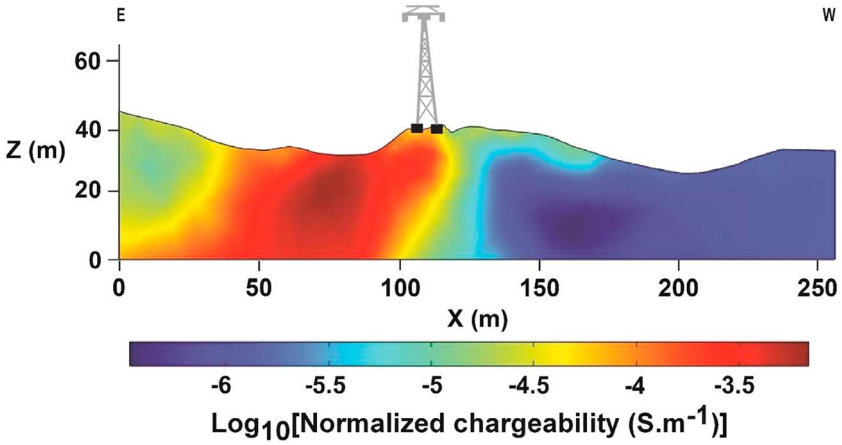

Figure 18. Two-dimensional cross section of normalized chargeability (Profile 1) extracted from the 3-D tomogram with the position of Pylon 2. The rock glacier is located on the right side and is characterized by very low normalized chargeability values.

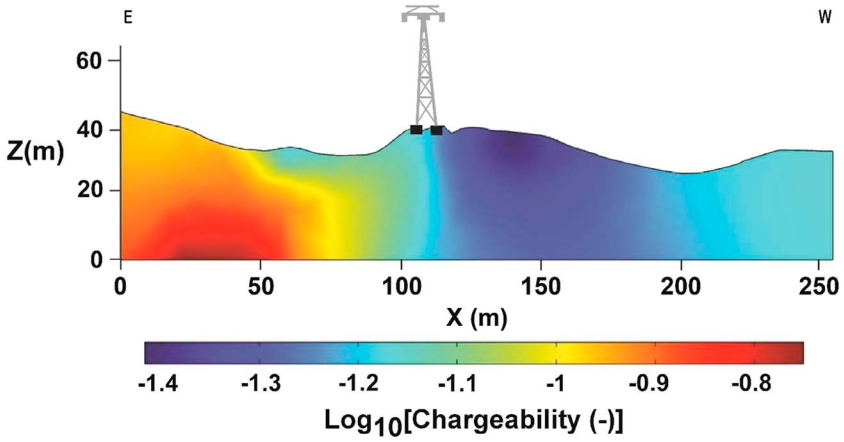

Figure 19. Two-dimensional cross section of chargeability (Profile 1) extracted from the 3-D tomogram with the position of Pylon 2. The chargeability is relatively uniform and close to the value of $R = 8 \times 10^{-2}$ (log $R = -1.1$).

(2017; see Figure 4). The slope is equal to $R = 8 \times 10^{-2}$, which is here again clearly independent of the temperature and saturation in agreement with equation (11). This finding has a very important implication: this proportionality reflects the fact that at low salinity, the electrical conductivity is dominated by the surface conductivity. In other words, electrical conductivity at the field site is dominated by surface conductivity.

5. Laboratory Investigation

5.1. Experimental Setup

While the temperature-resistivity relationship in the permafrost area has already been studied in the laboratory for rock slope environment (Krautblatter et al., 2010), chargeability calibration on superficial deposit samples is quite rare. With the exception of Wu et al. (2017), we are not aware of any work in this direction. In August 2017, we collected a single subsurface sediment sample on the rock glacier in the vicinity of Pylon 2 at a depth of 30 cm (volume: 2 L). Four liters of water from the melting of snow were also taken from a small lake at the site. The sample was first dried and then saturated under vacuum with this water. The porosity was determined by measuring the volume of material, its dry and water saturated weights. Its cation exchange capacity was measured with the cobalt hexamine method. We obtain a porosity of $\phi = 0.60$ and a cation exchange capacity CEC = 5.502 centimoles per kilogram (meq/100 g) = 5,300 C/kg (since 1 meq/100 g = 963.20 C/kg). The electrical conductivity of this water was made with a calibrated conductimeter and its conductivity was 0.010 S/m (at 25 °C). The core sample was saturated under vacuum with this

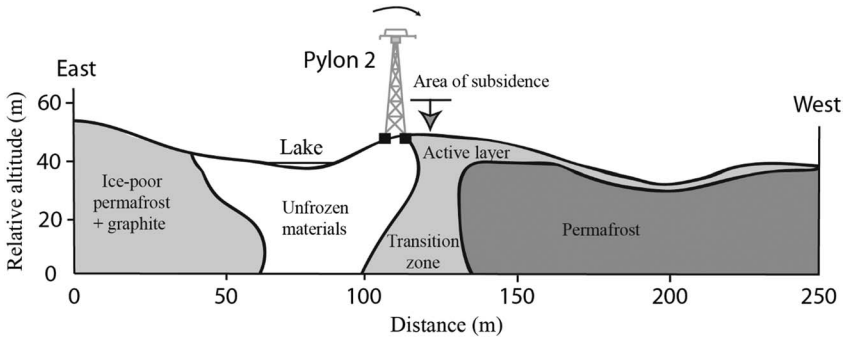

Figure 20. Interpretation of Profile 1 showing the permafrost and the seasonally unfrozen materials associated with the small lake along the 2-D geophysical profile. The area of subsidence associated with the degradation of the permafrost is likely responsible for the movement of the pylon. The thickness of the active layer is more significant near the pylon due to extensive earthworks.

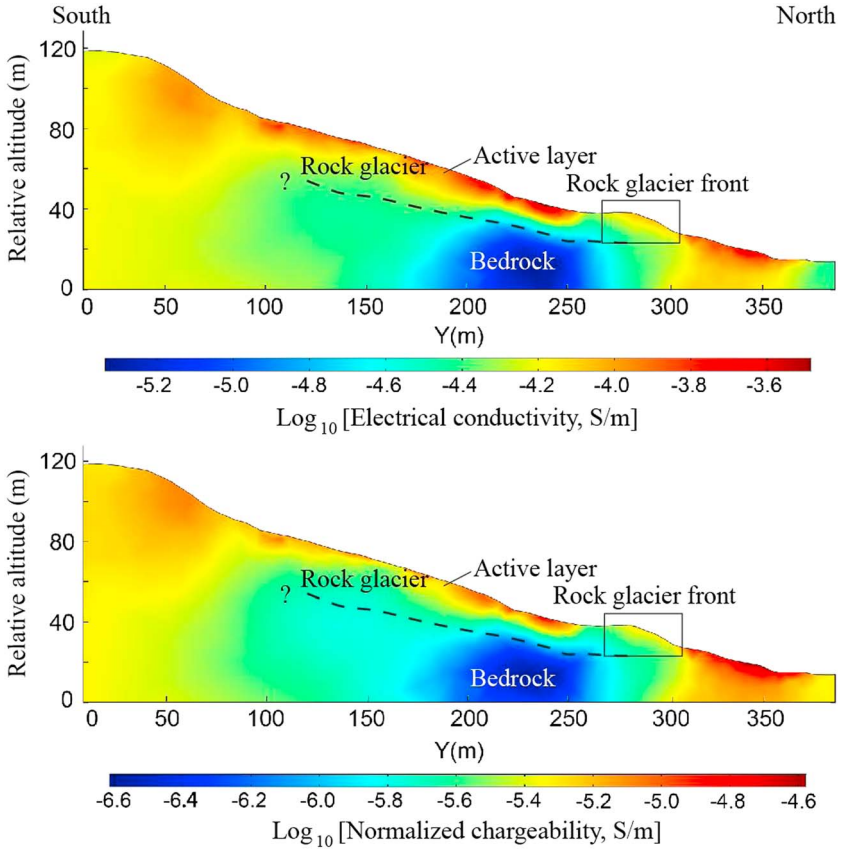

Figure 21. Two-dimensional cross section of conductivity and normalized chargeability (Profile 2) extracted from the 3-D tomogram and located on the rock glacier. The rock glacier is typically in the range $10^{-3.5}$ to $10^{-4.5}$ S/m, while the bedrock (graphitic schist) appears nearly more resistive with conductivity below 10^{-6} S/m because of the permafrost. Note that the color scale is different from Figures 17–19.

water. Then the sample was transferred in a 2.5-cm-diameter plastic tube, and four nonpolarizing Ag-$AgCl_2$ electrodes were set up: two (A and B) on the end-faces and two (M and N) along the core sample. The potential electrodes M and N were separated by a distance of 3.5 cm.

The sample holder was installed in a heat-resistant insulating bag immersed in a thermostat bath (KISS K6 from Huber, dimensions 210 × 400 × 546 mm, bath volume 4.5 L, see Figure 23a). The temperature of this bath is controlled with a precision of 0.1 °C. Glycol is used as heat carrying fluid and the complex conductivity measurements are done with the impedance meter shown in Figure 24b (see Zimmermann et al., 2007). At each temperature, we let enough time (>30 min, sometimes up to several hours, see Figure 23c) to the system to stabilize in temperature (thanks to a thermal probe placed in the sample holder). An additional check of the stabilization was done through repeated in-phase conductivity measurements until a plateau was reached.

The impedance meter is used to determine the complex conductivity σ^* written as

$$\sigma^* = \sigma' + i\sigma'' \ . \tag{21}$$

The in-phase conductivity σ' (in S/m) denotes the ability of the porous material to conduct electrical currents, while the quadrature (imaginary) conductivity σ'' (in S/m) characterizes the ability of the porous material to polarize (i.e., to store reversibly electrical charged under the influence of a primary electrical field). In absence of metallic particles, the quadrature conductivity and the normalized chargeability are linearly related to each other as discussed further below (see Revil et al., 2017, for further details).

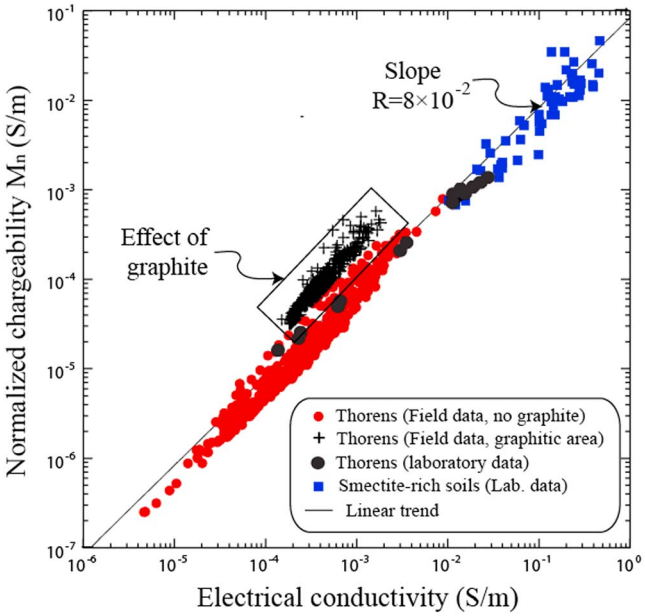

Figure 22. Normalized chargeability versus electrical conductivity at low pore water salinities. We did not consider the data in the unfrozen graphitic schist by using a chargeability threshold of 0.1. The smectite-rich-soil data are from Revil et al. (2017) and are shown in Figure 4. Data at low pore water conductivity (10^{-2} S/m at 25 °C). The value of the slope (equal to the dimensionless number $R = 8 \times 10^{-2}$) indicates that the conductivity is dominated by its surface conductivity contribution. Note that the data sets cover 6 orders of magnitude.

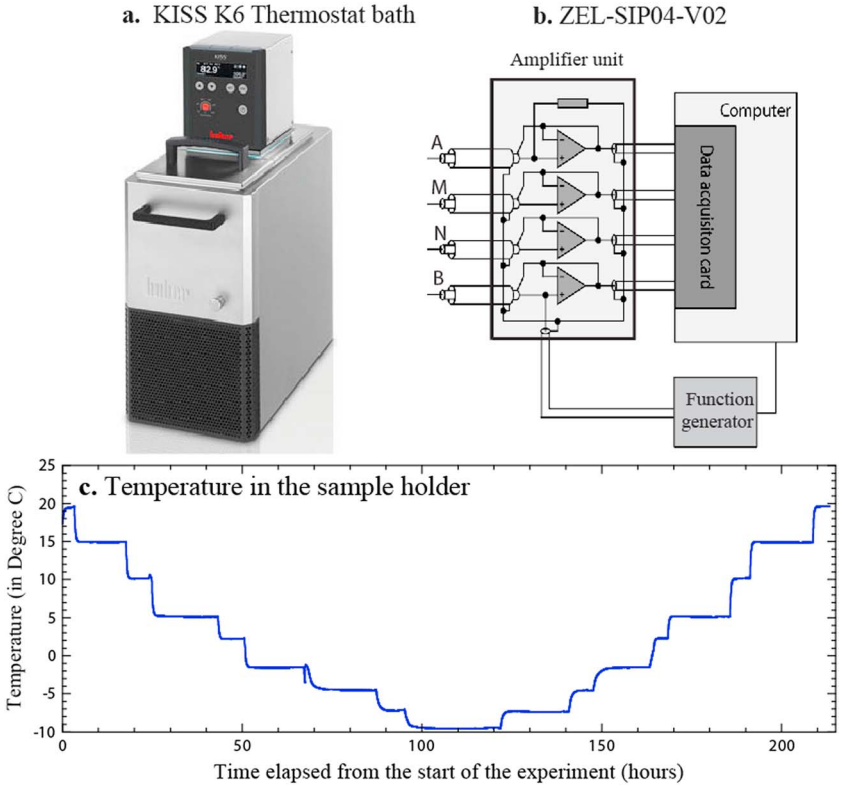

Figure 23. Equipment used for the laboratory experiment. (a) Thermostat bath (KISS K6 from Huber). (b) High-precision impedance meter with A and B being the current electrodes and M and N the voltage electrodes. The impedance meter was built by Egon Zimmerman (2007) and works in the frequency range 1 mHz to 45 kHz. (c) Temperature (in °C) in the sample holder during the course of the experiment.

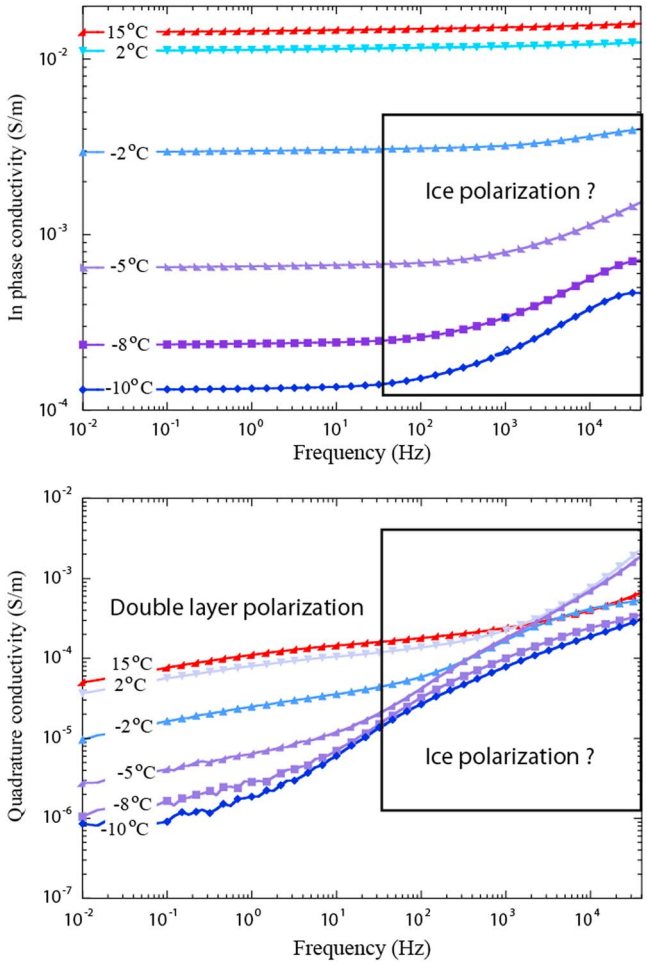

Figure 24. Complex conductivity spectra for the soil sample during freeze. We plot the in-phase and quadrature components of the complex conductivity versus the frequency of the input current. Note that there is a new dispersion phenomenon that starts to appear under freezing conditions, possibly associated with the polarization of ionic and Bjerrum defects in the ice itself. This polarization is superposed to the Maxwell-Wagner polarization mechanism. The lines are just guides to the eyes.

5.2. Results

Figure 24 shows the in-phase and quadrature conductivity spectra. The in-phase conductivity and quadrature conductivity can be related to electromigration and polarization, respectively. The low-frequency polarization ($<$1 kHz to 1 Hz depending on the temperature) are due to the relaxation of the electrical double layer as shown in Figures 2 and 3. Below 0 °C, a new polarization mechanism seems to appear that could be related to the Bjerrum defects in the ice (Bjerrum, 1952). The increase of the magnitude of this additional polarization effect seems indeed to be associated with decreasing temperature and therefore an increase in ice content.

Figures 25 and 26 show the temperature dependence of the in-phase conductivity with temperature above and below 0 °C. Above freezing conditions, the conductivity obeys a linear relationship with the temperature as observed in many studies (e.g., Revil et al., 1998 in which this temperature dependence was extended to +200 °C). The pore water and surface conductivities follow the following linear temperature dependence $\sigma_w(T) = \sigma_w(T_0)(1 + \alpha_w(T - T_0))$ and $\sigma_S(T) = \sigma_S(T_0)(1 + \alpha_S(T - T_0))$, respectively, and where T_0 denotes the reference temperature (T_0 = 25 °C), T is the temperature (in °C), and $\alpha_w \approx \alpha_S \approx 0.020 - 0.025/^{\circ}C$ (e.g., Revil et al., 2017; Vinegar & Waxman, 1984). Therefore, the temperature dependence of the complex conductivity itself is given by $\sigma^*(T) = \sigma^*(T_0)(1 + \alpha(T - T_0))$, where $\alpha = \alpha_w \approx \alpha_S$. These relationships mean that the temperature dependence of the in-phase and quadrature conductivities are due to the temperature dependences of the

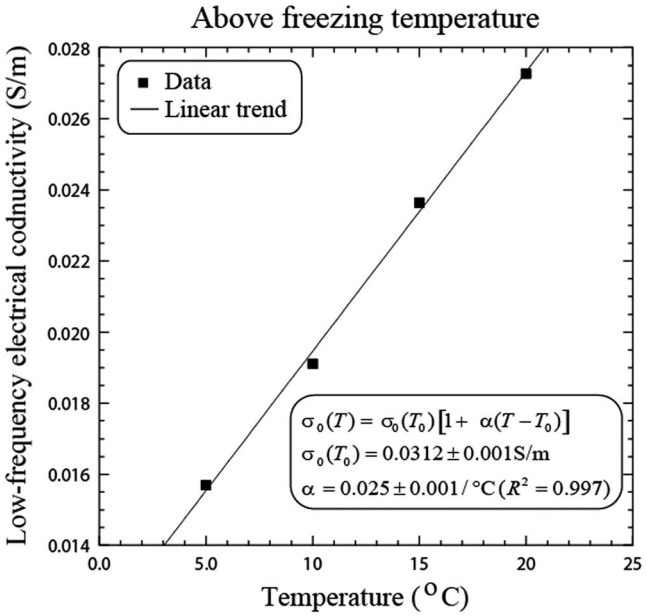

Figure 25. Electrical conductivity of the soil with a low pore water conductivity (low salinity). The linear temperature dependence provides a good fit to the experimental data as expected (see Revil et al., 1998).

mobilities of the charge carriers, which are in turn controlled by the temperature dependence of the (dynamic) viscosity of the pore water. Since the chargeability is a ratio of conductivities, this implies that the chargeability itself is temperature independent.

Below freezing conditions (0 °C in the present case), the temperature dependence is much stronger than the one discussed above. It can be fitted by an exponential growth relationship (Figure 26) as explained below. In these conditions, the mobility of the charge carriers remains temperature dependent (possibly with the same

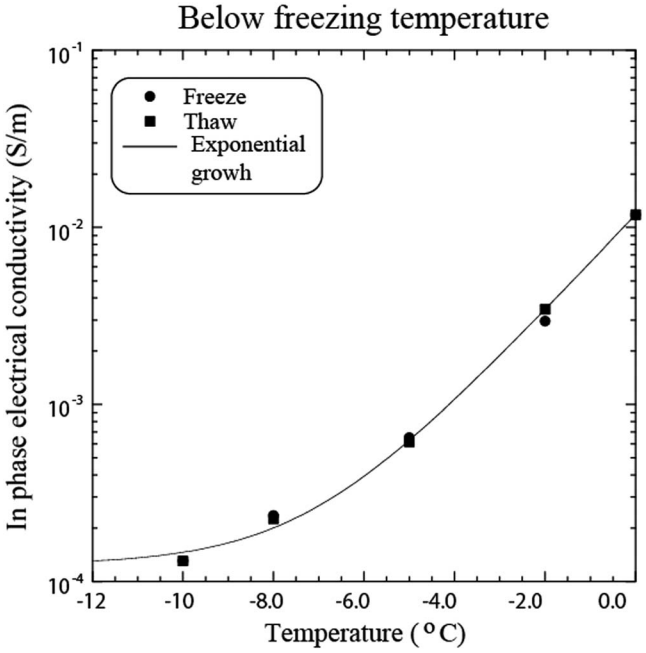

Figure 26. Electrical conductivity of the soil with a low pore water conductivity during freeze and thaw. An exponential growth model provides a good fit to the experimental data (see equation (23) of the main text). The result of the fit is discussed in the main text in terms of relevant parameters.

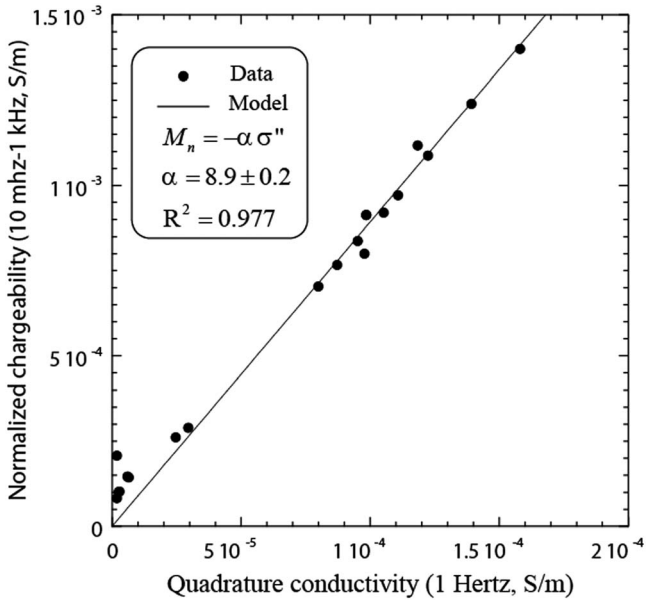

Figure 27. Normalized chargeability versus the absolute value of the quadrature conductivity. In the context of Drake's model (constant phase model), we expect a linear relationship between the normalized chargeability (determined from the dispersion of the conductivity curve) and the quadrature conductivity. Both parameters characterize the intrinsic polarization of the material.

temperature dependence than above). However, in addition, the saturation and salinity of the liquid water are changing with temperature. In order to simply model this effect, we assume that the conductivity is dominated by the surface conductivity (as discussed in section 4) and that the effect of temperature on the mobility is much smaller than the effect of temperature on the water content itself. This second assumption is easily proven by comparing the trends shown in Figures 25 and 26. The relationship between the water saturation and the temperature is called the *soil freezing curve*, and various soil freezing curves have been introduced in the literature (see discussion in Amiri et al., 2018). We introduce the following simple soil freezing curve for the water content:

$$\theta(T) = \varphi_m \exp\left(-\frac{T}{T_C}\right) + \theta_r. \tag{22}$$

where $\varphi_m = \phi - \theta_r$ denotes the maximum volumetric ice content at low temperature, ϕ denotes the porosity, θ_r the residual water content and where the temperature T and the critical temperature T_C are expressed in degree Celsius. Equation (22) is chosen in such a way it provides a fully liquid water saturated material at T = 0 °C (for a low salinity pore water) and a residual pore water at low temperatures (below 10 °C). With the previous assumptions, the electrical conductivity is given from equations (8) and (22) by

$$\sigma_\infty^b = \sigma_r \left[\frac{\varphi_m}{\theta_r} \exp\left(-\frac{T}{T_C}\right) + 1\right], \tag{23}$$

where the residual (surface) conductivity at low temperatures is given by $\sigma_r = \theta_r \rho_g B\,\mathrm{CEC}$, while at T = 0 °C, we have $\sigma_\infty^b = \phi \rho_g B\,\mathrm{CEC}$ (corresponding to the expression of the surface conductivity at full liquid water saturation). The fit shown in Figure 26 yields $\sigma_r = 1.2 \times 10^{-4}$ S/m, $\theta_r = 0.005$, and $T_C = -1.6$ °C and using a porosity of $\phi = 0.60$ (measured). Revil et al. (2018) obtained B (Na+, 25 °C) = 1.6×10^{-8} m^2 V^{-1} s^{-1} and a correction for temperature at −10 °C yields B (−10 °C) = 0.5×10^{-8} m^2 V^{-1} s^{-1}. Using CEC = 5,300 C/kg, θ_r = 0.005, ρ_g = 2,650 kg/m^3, and $B = 0.5 \times 10^{-8}$ m^2 V^{-1} s^{-1} in the formula $\sigma_r = \theta_r \rho_g B\,\mathrm{CEC}$ yields $\sigma_r = 3.5 \times 10^{-4}$ S/m in fair agreement with the value determined just above (1.2×10^{-4} S).

In Figure 27, we see that the normalized chargeability remains linear with the quadrature conductivity. Such dependence is expected for spectra showing a weak dependence with the frequency as shown here in Figure 24. This linear relationship is discussed in detail in Revil et al. (2017). We can define a linear relationship between the quadrature conductivity and the normalized chargeability:

$$\sigma'' \approx -\frac{M_n}{\alpha}. \tag{24}$$

The value of α will be determined using equations determined from the Drakes's model also called the *constant phase model* and is given in this case by

$$\alpha \approx \frac{2}{\pi} \ln A, \tag{25}$$

where A is the number of decades separating high and low frequencies. In our case we use conductivities taken at 10 mHz and 1 kHz, (so over five decades, i.e., $A = 10^5$). It follows that α = 7.3, that is, close to the observed value in Figure 27 (α = 8.9).

Finally, Figure 28 shows the quadrature conductivity at 1 Hz as a function of the instantaneous conductivity (taken at 10 kHz). We see that the quadrature conductivity (therefore the normalized chargeability and ipso facto the polarization) is proportional to the conductivity itself. As explained in the beginning of this paper, this can be done only if the conductivity is dominated by its surface conductivity contribution. This

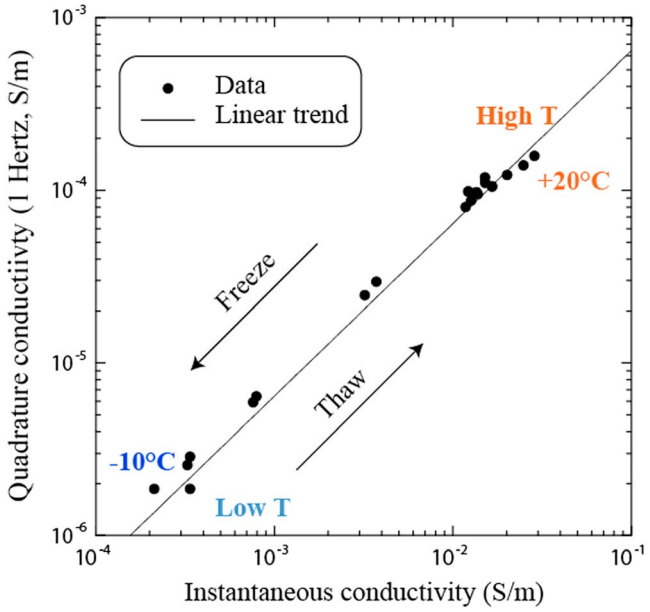

Figure 28. Quadrature conductivity (taken positive) versus the instantaneous conductivity of the soil undergoing freeze and thaw. The quadrature conductivity (hence the normalized chargeability) and the instantaneous conductivity are proportional to each other. This figure implies that the quadrature conductivity should follow an exponential growth curve with temperature (as in Figure 24).

demonstrates that the surface conductivity cannot be neglected in this type of experiment if the pore water salinity is low. In Figure 22, we added the laboratory data to the field data. At a given temperature, the values of the normalized conductivity and conductivity shown in Figure 22 are controlled by the value of the cation exchange capacity. However at a given CEC, the trend shown in Figure 22 below the freezing temperature is controlled by the temperature itself as shown in Figure 28.

6. Discussion

We discuss here the fundamental errors made by applied geophysicists in interpreting electrical resistivity/conductivity data on rock glaciers, permafrost landforms, and glaciers. In the dedicated literature, the conductivity model is taken as

$$\sigma' = \frac{1}{F}\sigma_w, \tag{26}$$

$$F = \phi^{-m}, \tag{27}$$

where m is called the *cementation exponent* in the literature and we prefer here the term *porosity exponent*. Three errors classically made are as follows: (1) Equation (26) is taken as a definition of the formation factor. (2) Equation (26) is called *Archie's law* instead of equation (27). In other words, a number of researchers called Archie's law an electrical conductivity equation instead of a relationship between the formation factor and the porosity (see, for instance, recently Perri et al., 2018). (3) Surface conductivity is neglected. Equation (26) should not be considered as defining the formation factor since it is only valid for high salinities, that is, salinities at which surface conductivity can be safely neglected. Equation (27) is Archie's law and is valid whatever the importance of surface conductivity σ_S in the more general conductivity equation

$$\sigma' = \frac{1}{F}\sigma_w + \sigma_S. \tag{28}$$

which is showing that the formation factor is not defined as the pore water conductivity divided by the conductivity of the medium. In our approach, we have demonstrated that if the ratio of the normalized chargeability by the (in-phase) conductivity is close to $R = 8 \times 10^{-2}$ (independent of temperature and saturation), then surface conductivity σ_S dominates the bulk conductivity contribution σ_w/F. From Figure 22, this was the case everywhere in the imaged volume with the exception of the graphite-rich area. So clearly, in the entire imaged volume, the surface conductivity dominates the bulk pore water contribution. Note also that when this is the case, the IP data do not bring new additional information to the electrical conductivity. In our approach, we did not have to assume that surface conductivity is dominant. This is a consequence of the unified conductivity/IP model developed by Revil (2012, 2013) and applied here to the interpretation of the laboratory and field data.

This brings on the table another interesting question. If equation (26) is used while the surface conductivity dominates, can we choose a pore water conductivity that would be equivalent to a surface conductivity? This reasoning would be also wrong. Indeed, the dependence on the water content of the bulk and surface conductivities are rather different (θ^2 vs. θ, respectively), and therefore, the use of the wrong equation cannot yield correct estimate of the water content or porosity, for instance, for the joint inversion of electrical resistivity and seismic data.

7. Conclusions

This is the first 3-D survey performed on a rock ice mixture combining electrical conductivity and chargeability tomography. The following conclusions have been reached.

1. A petrophysical model is proposed to model the chargeability (or normalized chargeability) of a complex mixture made of a background porous material (with some ice in the pore space) and embedded metallic particles. This chargeability model is versatile enough to consider the different cases of interest: ice-rich material, presence or absence of graphite in the rock, and the presence of clay minerals through their cation exchange capacity. This model is consistent with a variety of experimental data from the literature. The polarization model is based on the dynamic Stern layer concept for nonmetallic grains and the polarization of the intrinsic charge carriers of the metallic grains. Ice itself is probably characterized by its own polarization associated with charge defects, but this polarization appears as a rather high-frequency polarization mechanism (above 10 Hz) and is not observed at the period used for the time-domain IP measurements.
2. In the field and in the laboratory, the ratio of the normalized chargeability with the conductivity of the material is generally close to the predicted value, $R = 8 \times 10^{-2}$, which is independent of temperature and saturation in absence of metallic particles. In other words, when surface conductivity dominates the overall conductivity response, we expect that the chargeability is close to $R = 8 \times 10^{-2}$ and vice versa. In this case, the normalized chargeability is proportional to the conductivity itself. In this situation, IP does not necessarily bring new information to image the rock glacier itself except in demonstrating the dominant role of surface conductivity in the overall rock conductivity in such a case.
3. An additional series of laboratory experiments has been performed to understand the conductivity and normalized chargeability of a granular material from the field test site in order to see the influence of freeze and thaw. The measurements were carried out between +20 and −10 °C. They show the strong effect of saturation upon the conductivity below the freezing temperature. This effect can be captured by an exponential growth curve, which describes the relationship between the saturation and the temperature (soil freezing curve). The complex conductivity spectra indicate that a new polarization mechanism could be associated with the ice itself because of the migration of charge carriers inside the ice itself but only above 10 Hz. This is substantially higher than the field data that were acquired at a dominant frequency of ~1 Hz.

Acknowledgments
The first two authors contributed equally to this work. The authors gratefully acknowledge the SETAM (Société d'Exploitation des Téléphériques Tarentaise Maurienne) for the collaboration and all the geotechnical information given. We thank M. Marcer, K. Génuite, G. Heller, and A. Ollive for their help during the field survey. The numerical data and all the data used to generate the figures can be obtained by sending an email to the corresponding author (A. Revil, andre.revil@univ-smb.fr). They will be provided on ResearchGate upon the publication of the manuscript. We thank J. Poulenard for his help with the CEC measurement and X. Bodin and F. Magnin for fruitful discussions on the topic of the present paper. This study is part of FEDER POIA PermaRisk project and part of the transversal project "Ice and Fire". ISTerre is part of Labex OSUG@2020, and OSUG is thanked for funding the project RESOLVE. We thank the Associate Editor and the two anonymous referees for their very constructive and fruitful comments.

References

Amiri, E. A., Craiga, J. R., & Kurylyk, B. L. (2018). A theoretical extension of the soil freezing curve paradigm. *Advances in Water Resources*, *111*, 319–328. https://doi.org/10.1016/j.advwatres.2017.11.021

Archie, G. E. (1942). The electrical resistivity log as an aid in determining some reservoir characteristics. *Transactions of AIME*, *146*(01), 54–62. https://doi.org/10.2118/942054-G

Arenson, L., Hoelzle, M., & Springman, S. (2002). Borehole deformation measurements and internal structure of some rock glaciers in Switzerland. *Permafrost and Periglacial Processes*, *13*(2), 117–135. https://doi.org/10.1002/ppp.414

Arenson, L. U., & Jakob, M. (2017). Permafrost-related geohazards and infrastructure construction in mountainous environments. *Oxford Research Encyclopedia of Natural Hazard Science*, *30*. https://doi.org/10.1093/acrefore/9780199389407.013.292

Arenson, L. U., & Springman, S. M. (2005). Triaxial constant stress and constant strain rate tests on ice-rich permafrost samples. *Canadian Geotechnical Journal*, *42*(2), 412–430. https://doi.org/10.1139/t04-111

Beniston, M., Farinotti, D., Stoffel, M., Andreassen, L. M., Coppola, E., Eckert, N., et al. (2018). The European mountain cryosphere: A review of its current state, trends, and future challenges. *The Cryosphere*, *12*(2), 759–794. https://doi.org/10.5194/tc-12-759-2018

Bjerrum, N. (1952). Structure and properties of ice. *Science*, *115*(2989), 385–390. https://doi.org/10.1126/science.115.2989.385

Bodin, X., Krysiecki, J.-M., Schoeneich, P., Le Roux, O., Lorier, L., Echelard, T., et al. (2016). The 2006 collapse of the Bérard Rock Glacier (Southern French Alps). *Permafrost and Periglacial Processes*, *28*(1), 209–223. https://doi.org/10.1002/ppp.1887

Bodin, X., Thibert, E., Fabre, D., Ribolini, A., Schoeneich, P., Francou, B., et al. (2009). Two decades of responses (1986–2006) to climate by the Laurichard rock glacier, French Alps. *Permafrost Periglac Process*, *20*(4), 331–344. https://doi.org/10.1002/ppp.665

Broyden, C. G. (1965). A class of methods for solving nonlinear simultaneous equations. Mathematics of computation. *American Mathematical Society*, *19*(92), 577–593. https://doi.org/10.1090/S0025-5718-1965-0198670-6. JSTOR 2003941

Dafflon, B., Hubbard, S. S., Ulrich, C., & Peterson, J. E. (2013). Electrical Conductivity Imaging of Active Layer and Permafrost in an Arctic Ecosystem, through Advanced Inversion of Electromagnetic Induction Data. *Vadose Zone Journal*, *12*(4), vzj2012.0161. https://doi.org/10.2136/vzj2012.0161

Dafflon, B., Hubbard, S. S., Ulrich, C., Peterson, J. E., Wu, Y., Wainwright, H., & Kneafsey, T. (2016). Geophysical estimation of shallow permafrost distribution and properties in an ice-wedge polygon-dominated Arctic tundra region. *Geophysics*, *81*(1), WA247–WA263. https://doi.org/10.1190/geo2015-0175.1

Dahlin, T., Leroux, V., & Nissen, J. (2002). Measuring techniques in induced polarisation imaging. *Journal of Applied Geophysics*, *50*(3), 279–298. https://doi.org/10.1016/S0926-9851(02)00148-9

Daniels, J. J., Keller, G. V., & Jacobson, J. J. (1976). Computer-assisted interpretation of electromagnetic soundings over a permafrost section. *Geophysics*, *41*(4), 752–765. https://doi.org/10.1190/1.1440647

Debelmas, J. (1989). *Notice explicative de la carte géologique de Modane à 1/50000*. Orléans: BRGM.

Delaloye, R., Perruchoud, E., Avian, M., Kaufmann, V., Bodin, X., Hausmann, H., et al. (2008). Recent interannual variations of rock glacier creep in the European Alps, in: Proceedings of the 9th International Conference on Permafrost, Fairbanks, Alaska. Citeseer, 343–348.

Doetsch, J., Ingeman-Nielsen, T., Christiansen, A. V., Fiandaca, G., Auken, E., & Elberling, B. (2015). Direct current (DC) resistivity and induced polarization (IP) monitoring of active layer dynamics at high temporal resolution. *Cold Regions Science and Technology*, *119*, 16–28. https://doi.org/10.1016/j.coldregions.2015.07.002

Drzymala, J., Sadowski, Z., Holysz, L., & Chibowski, E. (1999). Ice/water interface: Zeta potential, point of zero charge, and hydrophobicity. *Journal of Colloid and Interface Science*, *220*(2), 229–234. https://doi.org/10.1006/jcis.1999.6528

Duvillard, P.-A., Ravanel, L., & Deline, P. (2015). Risk assessment of infrastructure destabilisation due to global warming in the high French Alps. *Revue de Géographie Alpine*, *103*(2). https://doi.org/10.4000/rga.2896

Emmert, A., & Kneisel, C. (2017). Internal structure of two alpine rock glaciers investigated by quasi-3-D electrical resistivity imaging. *The Cryosphere*, *11*(2), 841–855. https://doi.org/10.5194/tc-11-841-2017

Fabre, D., Cadet, H., Lorier, L., & Leroux, O. (2015). Detection of permafrost and foundation related problems in high mountain ski resorts. In G. Lollino, A. Manconi, J. Clague, W. Shan, & M. Chiarle (Eds.), *Engineering geology for society and territory—Volume 1: Climate change and engineering geology* (pp. 321–324). Cham: Springer International Publishing. https://doi.org/10.1007/978-3-319-09300-0_60

Florsch, N., Llubes, M., Téreygeol, F., Ghorbani, A., & Roblet, P. (2010). Quantification of slag heap volumes and masses through the use of induced polarization: Application to the Castel-Minier site. *Journal of Archaeological Science*, *38*(2), 438–451. https://doi.org/10.1016/j.jas.2010.09.027

Gardent, M., Rabatel, A., Dedieu, J.-P., & Deline, P. (2014). Multitemporal glacier inventory of the French Alps from the late 1960s to the late 2000s. *Global and Planetary Change*, *120*, 24–37. https://doi.org/10.1016/j.gloplacha.2014.05.004

Guillot, F. (1982). La vallée du Ponturin (Vanoise septentrionale, Alpes françaises). Mémoire de Géologie appliquée. L'université des sciences et techniques de Lille.

Haeberli, W. (1992). Construction, environmental problems and natural hazards in periglacial mountain belts. *Permafrost and Periglacial Processes*, *3*(2), 111–124. https://doi.org/10.1002/ppp.3430030208

Haeberli, W., Hallet, B., Arenson, L., Elconin, R., Humlum, O., Kääb, A., et al. (2006). Permafrost creep and rock glacier dynamics. *Permafrost and Periglacial Processes*, *17*(3), 189–214. https://doi.org/10.1002/ppp.561

Hartl, L., Fischer, A., Stocker-Waldhuber, M., & Abermann, J. (2016). Recent speed-up of an alpine rock glacier: An updated chronology of the kinematics of outer Hochebenkar rock glacier based on geodetic measurements. *Geografiska Annaler. Series A, Physical Geography*, *98*(2), 129–141. https://doi.org/10.1111/geoa.12127

Hauck, C., Böttcher, M., & Maurer, H. (2011). A new model for estimating subsurface ice content based on combined electrical and seismic data sets. *The Cryosphere*, *5*(2), 453–468. https://doi.org/10.5194/tc-5-453-2011

Hauck, C., & Kneisel, C. (Eds.) (2008). *Applied geophysics in periglacial environments*. Cambridge: Cambridge University Press. https://doi.org/10.1017/CBO9780511535628

Hauck, C., Vonder Mühll, D., & Maurer, H. (2003). Using DC resistivity tomography to detect and characterize mountain permafrost. *Geophysical Prospecting*, *51*(4), 273–284. https://doi.org/10.1046/j.1365-2478.2003.00375.x

Hilbich, C., Marescot, L., Hauck, C., Loke, M. H., & Mäusbacher, R. (2009). Applicability of electrical resistivity tomography monitoring to coarse blocky and ice-rich permafrost landforms. *Permafrost and Periglacial Processes*, *20*(3), 269–284. https://doi.org/10.1002/ppp.652

Ikeda, A., Matsuoka, N., & Kääb, A. (2008). Fast deformation of perennially frozen debris in a warm rock glacier in the Swiss Alps: An effect of liquid water. *Journal of Geophysical Research*, *113*, F01021. https://doi.org/10.1029/2007JF000859

Kääb, A., Frauenfelder, R., & Roer, I. (2007). On the response of rockglacier creep to surface temperature increase. *Global and Planetary Change*, *56*(1-2), 172–187. https://doi.org/10.1016/j.gloplacha.2006.07.005

Kellerer-Pirklbauer, A., & Kaufmann, V. (2017). Deglaciation and its impact on permafrost and rock glacier evolution: New insight from two adjacent cirques in Austria. *Science of The Total Environment*, *621*, 1397–1414. https://doi.org/10.1016/j.scitotenv.2017.10.087

Kemna, A., Binley, A., Cassiani, G., Niederleithinger, E., Revil, A., Slater, L., et al. (2012). An overview of the spectral induced polarization method for near-surface applications. *Near Surface Geophysics*, *10*(6), 453–468.

Kenner, R., Phillips, M., Beutel, J., Hiller, M., Limpach, P., Pointner, E., & Volken, M. (2017). Factors controlling velocity variations at short-term, seasonal and multiyear time scales, Ritigraben rock glacier, Western Swiss Alps. *Permafrost and Periglacial Processes*, *28*(4), 675–684. https://doi.org/10.1002/ppp.1953

Kneisel, C. (2004). New insights into mountain permafrost occurrence and characteristics in glacier forefields at high altitude through the application of 2D resistivity imaging. *Permafrost and Periglacial Processes*, *15*(3), 221–227. https://doi.org/10.1002/ppp.495

Kneisel, C., Emmert, A., & Kästl, J. (2014). Application of 3D electrical resistivity imaging for mapping frozen ground conditions exemplified by three case studies. *Geomorphology*, *210*(Supplement C), 71–82. https://doi.org/10.1016/j.geomorph.2013.12.022

Kneisel, C., Hauck, C., Fortier, R., & Moorman, B. (2008). Advances in geophysical methods for permafrost investigations. *Permafrost and Periglacial Processes*, *19*(2), 157–178. https://doi.org/10.1002/ppp.616

Krautblatter, M., Verleysdonk, S., Flores-Orozco, A., & Kemna, A. (2010). Temperature calibrated imaging of seasonal changes in permafrost rock walls by quantitative electrical resistivity tomography (Zugspitze, German/Austrian Alps). *Journal of Geophysical Research*, *115*, F02003. https://doi.org/10.1029/2008JF001209

Kummert, M., Delaloye, R., & Braillard, L. (2018). Erosion and sediment transfer processes at the front of rapidly moving rock glaciers: Systematic observations with automatic cameras in the western Swiss Alps. *Permafrost and Periglacial Processes*, *29*(1), 21–33. https://doi.org/10.1002/ppp.1960

Luethi, R., Phillips, M., & Lehning, M. (2017). Estimating non-conductive heat flow leading to intra-permafrost Talik Formation at the Ritigraben rock glacier (Western Swiss Alps): Estimating non-conductive heat flow. *Permafrost and Periglacial Processes*, *28*(1), 183–194. https://doi.org/10.1002/ppp.1911

Mansoor, N., & Slater, L. (2007). On the relationship between iron concentration and induced polarization in marsh soils. *Geophysics*, *72*(1), A1–A5. https://doi.org/10.1190/1.2374853

Marcer, M., Bodin, X., Brenning, A., Schoeneich, P., Charvet, R., & Gottardi, F. (2017). Permafrost Favorability Index: Spatial Modeling in the French Alps Using a Rock Glacier Inventory. *Frontiers in Earth Science*, *5*, 105. https://doi.org/10.3389/feart.2017.00105

Marcer, M., Serrano, C., Brenning, A., Bodin, X., Goetz, J., & Schoeneich, P. (2018). Inferring the destabilization susceptibility of mountain permafrost in the French Alps using an inventory of destabilized rock glaciers. *The Cryosphere Discussions*, 1–30. https://doi.org/10.5194/tc-2018-97

Maurer, H., & Hauck, C. (2007). Geophysical imaging of alpine rock glaciers. *Journal of Glaciology*, *53*(180), 110–120. https://doi.org/10.3189/172756507781833893

Mewes, B., Hilbich, C., Delaloye, R., & Hauck, C. (2017). Resolution capacity of geophysical monitoring regarding permafrost degradation induced by hydrological processes. *The Cryosphere*, *11*(6), 2957–2974. https://doi.org/10.5194/tc-11-2957-2017

PERMOS (2016). Permafrost in Switzerland 2010/2011 to 2013/2014. In J. Noetzli, R. Luethi, & B. Staub (Eds.), *Glaciological Report Permafrost No. 12–15 of the Cryospheric Commission of the Swiss Academy of Sciences* (85 pp.). Fribourg.

Perri, M. T., De Vita, P., Masciale, R., Portoghese, I., Chirico, G. B., & Cassiani, G. (2018). Time-lapse Mise-á-la-Masse measurements and modeling for tracer test monitoring in a shallow aquifer. *Journal of Hydrology*, *561*, 461–477. https://doi.org/10.1016/j.jhydrol.2017.11.013

Ping-Yu, C., Lian-Cheng, C., Shao-Yiu, H., Jui-Pin, T., & Wen-Fu, C. (2017). Estimating the hydrogeological parameters of an unconfined aquifer with the time-lapse resistivity-imaging method during pumping tests: Case studies at the Pengtsuo and Dajou sites, Taiwan. *Journal of Applied Geophysics*, *144*, 134–143.

Qi, Y., Soueid Ahmed, A., Revil, A., Ghorbani, A., Abdulsamad, F., Flosch, N., & Bonnenfant, J. (2018). Induced polarization response of porous media with metallic particles—Part 7. Detection and quantification of buried slag heaps. *Geophysics*, *83*(5), E277–E291. https://doi.org/10.1190/geo2017-0760.1

Revil, A. (2012). Spectral induced polarization of shaly sands: Influence of the electrical double layer. *Water Resources Research*, *48*, W02517. https://doi.org/10.1029/2011WR011260

Revil, A. (2013). On charge accumulations in heterogeneous porous materials under the influence of an electrical field. *Geophysics*, *78*(4), D271–D291. https://doi.org/10.1190/GEO2012-0503.1.

Revil, A., Abdel Aal, G. Z., Atekwana, E. A., Mao, D., & Florsch, N. (2015). Induced polarization response of porous media with metallic particles—Part 2. Comparison with a broad database of experimental data. *Geophysics*, *80*(5), D539–D552. https://doi.org/10.1190/GEO2014-0578.1

Revil, A., Cathles, L. M., Losh, S., & Nunn, J. A. (1998). Electrical conductivity in shaly sands with geophysical applications. *Journal of Geophysical Research*, *103*(B10), 23,925–23,936. https://doi.org/10.1029/98JB02125

Revil, A., Coperey, A., Deng, Y., Cerepi, A., & Seleznev, N. (2018). Complex conductivity of tight sandstones. *Geophysics*, *83*(2), E55–E74. https://doi.org/10.1190/GEO2017-0096.1

Revil, A., Coperey, A., Shao, Z., Florsch, N., Fabricius, I. L., Deng, Y., et al. (2017). Complex conductivity of soils. *Water Resources Research*, *53*, 7121–7147. https://doi.org/10.1002/2017WR020655

Revil, A., Florsch, N., & Mao, D. (2015). Induced polarization response of porous media with metallic particles—Part 1: A theory for disseminated semiconductors. *Geophysics*, *80*(5), D525–D538. https://doi.org/10.1190/GEO2014-0577.1

Scapozza, C., & Laigre, L. (2014). The contribution of electrical resistivity tomography (ERT) in alpine dynamics geomorphology: Case studies from the Swiss Alps. *Géomorphologie: Relief, Processus, Environnement*, *20*(1), 27–42. https://doi.org/10.4000/geomorphologie.10474

Scherrer, S. C., Fischer, E. M., Posselt, R., Liniger, M. A., Croci-Maspoli, M., & Knutti, R. (2016). Emerging trends in heavy precipitation and hot temperature extremes in Switzerland: Trends in Swiss climate extremes. *Journal of Geophysical Research: Atmospheres*, *121*, 2626–2637. https://doi.org/10.1002/2015JD024634

Schoeneich, P., Dall'Amico, M., Deline, P., & Zischg, A. (2011), Hazards related to permafrost and to permafrost degradation. PermaNET project, state-of-the-art report 6.2. On-Line Publication ISBN 978–2–903095-59-8.

Scott, W., Sellmann, P., & Hunter, J. (1990). Geophysics in the study of permafrost. In *Geotechnical and environmental geophysics*, 1, 355–384. https://doi.org/10.1190/1.9781560802785.ch13

Scotti, R., Crosta, G. B., & Villa, A. (2017). Destabilisation of creeping permafrost: The Plator rock glacier case study (Central Italian Alps). *Permafrost and Periglacial Processes*, *28*(1), 224–236. https://doi.org/10.1002/ppp.1917

Seigel, H. O. (1959). Mathematical formulation and type curves for induced polarization. *Geophysics*, *24*(3), 547–565. https://doi.org/10.1190/1.1438625

Shuey, R. T., & Johnson, M. (1973). On the phenomenology of electrical relaxation in rocks. *Geophysics*, *38*(1), 37–48. https://doi.org/10.1190/1.1440331

Slater, L. D., & Glaser, D. R. (2003). Controls on induced polarization in sandy unconsolidated sediments and application to aquifer characterization. *Geophysics*, *68*(5), 1547–1558. https://doi.org/10.1190/1.1620628

Soueid Ahmed, A., Revil, A., Byrdina, S., Coperey, A., Gailler, L., Grobbe, N., et al. (2018). 3D electrical conductivity tomography of volcanoes. *Journal of Volcanology and Geothermal Research*, *356*, 243–263.

Soueid Ahmed, A., Revil, A., Jardani, A., & Chen, R. (2018). 3D geostatistical inversion of induced polarization data and its application to coal seam fires. *Geophysics*, *83*(3), 1–59.

Springman, S. M., Arenson, L. U., Yamamoto, Y., Maurer, H., Kos, A., Buchli, T., & Derungs, G. (2012). Multidisciplinary investigations on three rock glaciers in the Swiss Alps: Legacies and future perspectives. *Geografiska Annaler. Series A, Physical Geography*, *94*(2), 215–243. https://doi.org/10.1111/j.1468-0459.2012.00464.x

Springman, S. M., Yamamoto, Y., Buchli, T., Hertrich, M., Maurer, H., Merz, K., et al. (2013). Rock glacier degradation and instabilities in the European Alps: A characterisation and monitoring experiment in the Turtmanntal, CH. In C. Margottini, P. Canuti, & K. Sassa (Eds.), *Landslide Science and Practice* (pp. 5–13). Berlin, Heidelberg: Springer Berlin Heidelberg. https://doi.org/10.1007/978-3-642-31337-0_1

Supper, R., Ottowitz, D., Jochum, B., Römer, A., Pfeiler, S., Kauer, S., et al. (2014). Geoelectrical monitoring of frozen ground and permafrost in alpine areas: Field studies and considerations towards an improved measuring technology. *Near Surface Geophysics*, *12*(2007), 93–115. https://doi.org/10.3997/1873-0604.2013057

Thompson, S., Kulssa, B., & Luckman, A. (2012). Integrated electrical resistivity tomography (ERT) and self-potential (SP) techniques for assessing hydrological processes within glacial lake moraine dams. *Journal of Glaciology*, *58*(211), 849–858. https://doi.org/10.3189/2012JoG11J235

Timur, A. (1968). Velocity of compressional waves in porous media at permafrost temperatures. *Geophysics*, *33*(4), 584–595. https://doi.org/10.1190/1.1439954

Vinegar, H. J., & Waxman, M. H. (1984). Induced polarization of shaly sands. *Geophysics*, *49*(8), 1267–1287. https://doi.org/10.1190/1.1441755

Waxman, M. H., & Smits, L. J. M. (1968). Electrical conductivities in oil bearing shaly sands. *SPE Journal*, *8*, 107–122.

Weller, A., Nordsiek, S., & Debschütz, W. (2010). Estimating permeability of sandstone samples by nuclear magnetic resonance and spectral-induced polarization. *Geophysics*, *75*(6), E215–E226. https://doi.org/10.1190/1.3507304

Weller, A., & Slater, L. (2012). Salinity dependence of complex conductivity of unconsolidated and consolidated materials: Comparisons with electrical double layer models. *Geophysics*, *77*(5), D185–D198. https://doi.org/10.1190/geo2012-0030.1

Weller, A., Slater, L., & Nordsiek, S. (2013). On the relationship between induced polarization and surface conductivity: Implications for petrophysical interpretation of electrical measurements. *Geophysics*, *78*(5), D315–D325. https://doi.org/10.1190/GEO2013-0076.1

Wu, Y., Nakagawa, S., Kneafsey, T. J., Dafflon, B., & Hubbard, S. (2017). Electrical and seismic response of saline permafrost soil during freeze-thaw transition. *Journal of Applied Geophysics*, *146*, 16–26. https://doi.org/10.1016/j.jappgeo.2017.08.008

Zimmermann, E., Berwix, J., Glaas, W., Meier, H., Münch, H.M., & Kemna, A. (2007). ZEL-SIP04-V02: User manual, Forschungszentrum Julich GmbH.